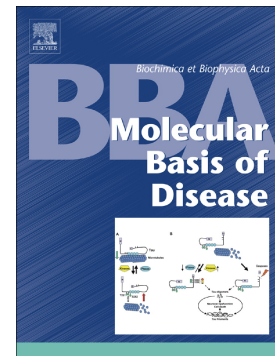


Accepted Manuscript

Deciphering OPA1 mutations pathogenicity by combined analysis of human, mouse and yeast cell models

Valentina Del Dotto, Mario Fogazza, Francesco Musiani, Alessandra Maresca, Serena J. Aleo, Leonardo Caporali, Chiara La Morgia, Cecilia Nolli, Tiziana Lodi, Paola Goffrini, David Chan, Valerio Carelli, Michela Rugolo, Enrico Baruffini, Claudia Zanna



PII: S0925-4439(18)30289-8
DOI: doi:[10.1016/j.bbadis.2018.08.004](https://doi.org/10.1016/j.bbadis.2018.08.004)
Reference: BBADIS 65210
To appear in: *BBA - Molecular Basis of Disease*
Received date: 12 January 2018
Revised date: 24 July 2018
Accepted date: 1 August 2018

Please cite this article as: Valentina Del Dotto, Mario Fogazza, Francesco Musiani, Alessandra Maresca, Serena J. Aleo, Leonardo Caporali, Chiara La Morgia, Cecilia Nolli, Tiziana Lodi, Paola Goffrini, David Chan, Valerio Carelli, Michela Rugolo, Enrico Baruffini, Claudia Zanna , Deciphering OPA1 mutations pathogenicity by combined analysis of human, mouse and yeast cell models. *Bbadis* (2018), doi:[10.1016/j.bbadis.2018.08.004](https://doi.org/10.1016/j.bbadis.2018.08.004)

This is a PDF file of an unedited manuscript that has been accepted for publication. As a service to our customers we are providing this early version of the manuscript. The manuscript will undergo copyediting, typesetting, and review of the resulting proof before it is published in its final form. Please note that during the production process errors may be discovered which could affect the content, and all legal disclaimers that apply to the journal pertain.

**Deciphering *OPAI* mutations pathogenicity by combined analysis of
human, mouse and yeast cell models**

Valentina Del Dotto,¹ Mario Fogazza,² Francesco Musiani,² Alessandra Maresca,³ Serena J. Aleo,²
Leonardo Caporali,³ Chiara La Morgia,^{1,3} Cecilia Nolli,⁴ Tiziana Lodi,⁴ Paola Goffrini,⁴ David
Chan,⁵ Valerio Carelli,^{1,3} Michela Rugolo,² Enrico Baruffini,^{4,6} and Claudia Zanna,^{2,6,*}

¹Unit of Neurology, Department of Biomedical and NeuroMotor Sciences (DIBINEM), University
of Bologna, 40139 Bologna, Italy;

²Department of Pharmacy and Biotechnology (FABIT), University of Bologna, 40126 Bologna,
Italy;

³IRCCS Institute of Neurological Sciences of Bologna, Bellaria Hospital, 40139 Bologna, Italy;

⁴Department of Chemistry, Life Sciences and Environmental Sustainability, University of Parma,
43124 Parma, Italy;

⁵Division of Biology and Biological Engineering, California Institute of Technology (CALTECH),
Pasadena, CA 91125, USA;

⁶Co-senior authors

*Corresponding author:

Claudia Zanna, PhD

Department of Pharmacy and Biotechnologies (FABIT), University of Bologna,

Via Selmi 3, 40126 Bologna, Italy

Tel +390512091286; email claudia.zanna76@gmail.com

ABSTRACT

OPA1 is the major gene responsible for Dominant Optic Atrophy (DOA) and the syndromic form DOA “plus”. Over 370 *OPA1* mutations have been identified so far, although their pathogenicity is not always clear. We have analyzed one novel and a set of known *OPA1* mutations to investigate their impact on protein functions in primary skin fibroblasts and in two “ad hoc” generated cell systems: the MGM1/*OPA1* chimera yeast model and the *Opal*^{-/-} MEFs model expressing the mutated human *OPA1* isoform 1. The yeast model allowed us to confirm the deleterious effects of these mutations and to gain information on their dominance/recessivity. The MEFs model enhanced the phenotypic alteration caused by mutations, nicely correlating with the clinical severity observed in patients, and suggested that the DOA “plus” phenotype could be induced by the combinatorial effect of mitochondrial network fragmentation with variable degrees of mtDNA depletion. Overall, the two models proved to be valuable tools to functionally assess and define the deleterious mechanism and the pathogenicity of novel *OPA1* mutations, and useful to testing new therapeutic interventions.

Keywords: OPA1 mutations, Dominant Optic Atrophy (DOA), OPA1, mitochondrial network, mtDNA, mitochondrial functions

1. INTRODUCTION

Dominant optic atrophy (DOA) is one of the most common inherited optic neuropathies, characterized by degeneration of the retinal ganglion cells, leading to optic nerve atrophy and ultimately to blindness [1,2]. Most DOA patients harbor mutations in the *OPA1* gene [3,4] encoding the mitochondrial GTPase OPA1, localized in the inner mitochondrial membrane [5]. This protein displays a mitochondrial-targeting sequence, a predicted transmembrane domain, followed by the three highly conserved regions: the GTPase, the middle and the GTPase effector domains. Eight OPA1 variants are present in humans, undergoing proteolytic cleavage by YME1L and OMA1 proteases [6] and generating a mixture of long and short isoforms (l- and s-forms) anchored to the inner membrane or soluble, respectively [7,8].

Currently, over 370 *OPA1* gene variants have been identified, of which 65% is considered pathogenic. About 50% of the pathogenic variants cause the premature truncation of the open reading frame [9], supporting haploinsufficiency as the main pathological mechanism of the disease. The missense variants, mostly clustered in the GTPase domain and envisaged to exert a dominant-negative effect [10], are associated with high risk to developing the severe multisystem disorder DOA “plus” characterized by additional extraocular features, including sensorineural deafness, ataxia, myopathy, chronic progressive external ophthalmoplegia, peripheral neuropathy, multiple sclerosis-like features and parkinsonism/dementia [11–15]. More recently, severe clinical phenotypes, ranging from Behr to Leigh syndromes, have been associated with compound heterozygosity of *OPA1* mutations, frequently in combination with the I382M hypomorphic allele, or homozygous *OPA1* mutations qualifying as recessive forms [16–20].

Different degrees of mitochondrial network fragmentation and *cristae* disorganization have been reported in fibroblasts [11,21–24] and skeletal muscle from DOA patients [11], as well as in DOA mouse models [25–27].

Phosphorus magnetic resonance spectroscopy revealed *in vivo* defective oxidative phosphorylation (OXPHOS) with reduced ATP production in muscle of DOA patients with several nonsense and

missense *OPA1* mutations [28,29]. Dysfunctions of the energetic metabolism, i.e. decreased ATP synthesis rate, respiratory complexes activities, oxygen consumption and membrane potential were also documented in fibroblasts and lymphoblasts of patients carrying different *OPA1* mutations [21,23,24,30].

Mitochondrial DNA (mtDNA) depletion was never reported in fibroblasts or skeletal muscles of DOA and DOA “plus” patients [11,12,24,31], showing rather increased mtDNA copy number in COX-negative fibers [13]. Conversely, mtDNA deletions, initially associated with the severe DOA “plus” phenotype only [11,31], were subsequently reported in skeletal muscles of the majority of patients harboring *OPA1* mutations, even in those with non-syndromic DOA [29]. Only recently, the identification of families with truly recessive *OPA1* mutations and affected with a multisystem disorder, documented the occurrence of mtDNA depletion in skeletal muscle [18].

It is noteworthy that primary skin fibroblasts derived from patients bearing *OPA1* mutations represent an important cell model for studying DOA pathophysiology, even if they often reveal a rather mild phenotype, likely as a consequence of the hemizygous transmission of DOA and the type/position of the mutation. Therefore, cell models avoiding the partial compensatory effect of the wild-type allele would enhance the defective phenotypic profile of the pathogenic *OPA1* mutant allele. To this end, we developed two different cell models. The first is the Mgm1/*OPA1* chimera yeast model, that has been previously described in detail [32]. The second takes advantage of *Opa1*^{-/-} mouse embryonic fibroblasts (MEFs), where human *OPA1* isoform 1 (ISO1) bearing *OPA1* mutations was expressed. The strength of these two models is that they are designed to provide complementary and non-overlapping information, thus allowing for a quick and comprehensive analysis of *OPA1* mutations pathophysiology. Here we present the detailed molecular and functional characterization of fibroblasts, MEFs and MGM1/*OPA1* chimeras, demonstrating a faithful genotype/phenotype correlation, associating the DOA “plus” phenotype with a combinatorial effect of mitochondrial network fragmentation and mtDNA depletion, and validating a novel *OPA1* mutation.

2. MATERIALS AND METHODS

2.1. Plasmid construction and retroviral transduction

Plasmid expressing the OPA1 isoforms 1 [7] was further mutagenized (I382M and D603H) and cloned into the pMSCV-puro vector, whereas the plasmids expressing isoform 1 bearing the mutations G439V and R445H were previously described [33]. Retrovirus production and infection were performed as described previously [34]. Plasmid (6 μ g/experiment) transfection of mouse embryonic fibroblasts (MEFs) was performed with Lipofectamine 3000 (Life Technologies) following the manufacturer's instructions.

2.2. Cells and culture conditions

Skin fibroblast were derived, following informed consent, from five healthy donors, two DOA patients from two unrelated families with the I382M mutation, one patient with the G439V mutation, two related patients with the R445H mutation and two related patients with the D603H mutation. *OPA1* gene localization of these mutations is reported in Table 1. All mutations were heterozygous and strictly co-segregated with individuals affected by optic atrophy in families with autosomal dominant inheritance.

The range of age for patients' fibroblasts is 24-59 years and for controls' fibroblasts is 24-60 years, with 3 men and 2 women. Matching healthy donors with DOA patients for age and sex, the behavior of the five controls used was very similar and we decided to pull the controls together.

Fibroblasts and MEFs were grown in DMEM containing 25mM glucose supplemented with 10% fetal bovine serum (FBS, South America, Gibco, Life Technologies), 2mM L-glutamine, 100U/ml penicillin and 100 μ g/ml streptomycin, in an incubator with a humidified atmosphere of 5% CO₂ at 37°C. For some experiments, cells were grown in glucose-free DMEM supplemented with 5mM galactose, 5mM sodium pyruvate and 5% FBS (DMEM-galactose).

2.3. Cellular ATP content

The ATP content of cells in DMEM and during incubation in DMEM-galactose was measured by using the luciferin/luciferase assay, as previously described [35]. For statistical analysis, the Dunnett's multiple comparison test was used.

2.4. Mitochondrial network morphology

Mitochondrial network morphology was analyzed as previously described in [36]. For statistical analysis, the Dunnett's multiple comparison test was used.

2.5. mtDNA content

Quantification of human mtDNA copy number relative to nuclear DNA (nDNA) was performed, for both fibroblasts and muscle tissue, as previously described [37]. Quantification of mouse mtDNA copy number relative to nuclear DNA (nDNA) was carried out amplifying both mt-Nd1 and β -Globin. Quantification was performed using the $\Delta\Delta C(t)$ method. Primer sequences are reported in supplementary materials. For statistical analysis, the Dunnett's multiple comparison test was used.

2.6. Oxygen consumption rate

The OCR was measured in XFe24 Extracellular Flux Analyzer (Seahorse Bioscience). Oxygen concentration were measured under basal condition and after injection of 1 μ M oligomycin, 1 μ M carbonyl cyanide 4-(trifluoromethoxy) phenylhydrazone (FCCP) or 5 μ M carbonyl cyanide m-chlorophenyl hydrazone (CCCP), 1 μ M rotenone and 1 μ M antimycin A. The OCR values (pmoles O_2 /min) were normalized for protein content of each well, determined by the SRB assay. For statistical analysis, the Dunnett's multiple comparison test was used.

2.7. Western blotting

Cell lysates were prepared as previously described [24]. Aliquots were separated by 8% SDS-PAGE and transferred onto nitrocellulose membranes (Bio-Rad). The membranes were incubated overnight at 4°C with the primary antibodies, then visualized using horseradish peroxidase-conjugated secondary antibodies. The chemiluminescence signals were revealed using an ECL Western blotting kit and measured with Gel Logic 1500 Imaging System, Biosense. For statistical analysis, the Dunnett's multiple comparison test was used.

2.8. Respiratory supercomplexes and Complex V analysis

Supercomplexes were separated by Blue Native-PAGE and analyzed as previously described [36]. For statistical analysis, the Dunnett's multiple comparison test was used.

2.9. cDNA Sequencing

Total RNA was extracted from fibroblasts using the Pure Link RNA mini kit (Ambion) and treated with DNaseI enzyme (Sigma Aldrich). 1 µg of RNA was reverse transcribed by SuperScript VILO cDNA synthesis kit and analyzed by Sanger Sequencing, as previously reported [38].

2.10. Yeast strains and media

The yeast strains used in this work were W303-1A Δ *mgm1* (*MATa leu2-3, trp1-1, can1-100, ura3-1, ade2-1, his3-11 mgm1::KanR*), W303-1B Δ *mgm1* (*MATa leu2-3, trp1-1, can1-100, ura3-1, ade2-1, his3-11 mgm1::KanR*). The diploid DW1.1 was obtained by crossing W303-1A Δ *mgm1* and W303-1B Δ *mgm1* [32]. Synthetic complete medium (SC) contained 6.9g/l yeast nitrogen base without amino acids (Formedium), 1g/l drop-out mix according to Kaiser et al. [39]. YP medium contained 0.5% yeast extract (Formedium) and 1% peptone (Formedium); YPA medium was YP 2X supplemented with 40mg/ml adenine base (Formedium). Carbon sources were added as indicated in the text.

2.11. Plasmids and construction of strains harboring *CHIM3* wt and mutant alleles

The plasmids used in this work are pFL38TEToff, pFL39TEToff, pFL36TEToff, pFL38MGM1 and pFL39MGM1 [32]. *chim3* mutant alleles were obtained by site-directed mutagenesis of a *CHIM3* gene fragment, using the overlap extension technique [40]. In the first PCR, the forward primer TATACYC1Fw and specific reverse mutagenic primers were used (see primers list in the supplementary materials). In the second PCR, specific forward mutagenic primers and the reverse primer MGMOPACNotRv were employed. The final mutagenized products were obtained by using the overlapping PCR fragments as templates, with TATACYC1Fw and MGMOPACNotRv as external primers. Each final product was then digested with *NotI* and cloned in *NotI*-digested pFL39TEToff, obtaining pFL39TEToff plasmid-borne *CHIM3*^{S298N}, *CHIM3*^{G300E}, *CHIM3*^{L331P}, *CHIM3*^{G439V}, *CHIM3*^{T449P}, *CHIM3*^{S545R}, *CHIM3*^{L593P}, *CHIM3*^{D603H}, *CHIM3*^{Q785R} and *CHIM3*^{V910D} mutant alleles. *Mgm1* mutant alleles were obtained in the same way, using the forward primer MGM1FwSall and the reverse primer MGM1RvSacI together with mutagenic primers reported in supplementary materials. Mutant and wt *CHIM3* alleles were introduced in the Δ *mgm1* strain through the plasmid shuffling technique as previously reported [41].

2.12. Complementation studies in yeast

Oxidative growth was evaluated by spotting serial cell dilutions of haploid strains (5×10^4 , 5×10^3 , 5×10^2 and 5×10^1 cell/spot), in a total volume of 5 μ l on YP medium, supplemented with either 2% glucose or 2% glycerol after a 5-days incubation at 28°C. Diploid strains were diluted to an initial concentration of 5 OD and then four 10-fold serial dilutions were made. A total volume of 5 μ l was spotted on solid SC medium, supplemented with 2% glucose or 1.5% glycerol-1.5% ethanol and the growth was evaluated after a 7-days incubation at 28°C.

To measure the respiratory activity, diploid strains were pre-grown in SC supplemented with 2% galactose for 48h to limit the growth of *petite* cells. Cells were inoculated at a final concentration of 0.08 OD/ml in SC supplemented with 0.6% glucose and grown until glucose was exhausted for

approximately 20h. The OCR was measured on whole cells using a Clark-type oxygen electrode (Oxygraph System Hansatech Instruments England) with 1ml of air-saturated respiration buffer (0.1M phthalate–KOH, pH 5.0), 10mM glucose at 30°C. The reaction started by addition of 20mg of wet-weight cells, as described previously [42,43]. For statistical analysis, the Dunnett's multiple comparison test was used.

2.13. Western blot analysis in yeast

Total proteins from 4.8 OD (for haploid strains) and 3.6 OD (for diploid strains) of cells grown in SC supplemented with 0.6% glucose until exhaustion were extracted with the trichloroacetic acid (TCA) method by chilling the cells supplemented with 120 mM NaOH, 0.5% β -mercaptoethanol, 650 μ M PMSF and 25% TCA on ice, then re-suspending the proteins in 60 μ l of Laemmli sample buffer at pH 6.8. 10 μ l of such suspension were separated by 8% SDS-PAGE, and electro-blotted onto nitrocellulose filters which were then incubated with anti-OPA1 and anti-VDAC antibodies. After incubation with anti-mouse secondary antibodies, the chemiluminescence signals were revealed using by ECL Western blotting substrate and measured with Imagequant Software (GE Healthcare).

2.14. Mitochondrial morphology in yeast

Haploid and diploid strains carrying *CHIM3* or *chim3* mutant alleles were transformed with pYEF1mtGFP [32]. Cells were pre-grown in SC medium supplemented with 2% glucose. After 24h, the cells were transferred to SC medium supplemented with 0.15% glucose and 2% galactose in order to induce the expression of mtGFP, until the mid-log phase was reached. Once adjusted to 1 OD/ml, the cells were observed with a Zeiss Observer 2.1 fluorescence microscope using a 630X magnification and images captured using an AxioVision Rel 4.8 software. Statistical analysis was performed using a χ^2 test on a 2x2 contingency table comparing the number of cells with filamentous mitochondria vs the number of cells with giant or fragmented mitochondria.

2.15. Template search, sequence alignments, and OPA1 homology modeling

Template search was performed using the HHsearch method employed by the HHpred server (doi:10.1093/nar/gki408). The server performs up to eight iterative PSI-BLAST (doi:10.1093/nar/25.17.3389) searches through filtered versions of the non-redundant (nr) database from the NCBI. Using the final target alignment a profile hidden Markov model (HMM) (doi:10.1006/jmbi.1994.1104 ; doi:10.1093/bioinformatics/14.9.755) is calculated. Homologous templates are identified by searching through a weekly updated database containing HMMs for a representative subset of PDB sequences. Finally, HHsearch ranks database matches by the probability of the match to be homologous to the target sequence. This is useful to distinguish homologous from non-homologous matches. Excluding PDB structures that were not solved by using X-ray crystallography, HHpred identified the human myxovirus resistance protein 1 (MxA), an interferon-induced dynamin-like GTPase and the human Dynamin 1-like protein (DNM1L) as the best templates for OPA1.

The target and template sequences were realigned using the Promals3D server (doi:10.1093/nar/gkn072) (see Supplementary Information for the results of the alignment). The obtained alignment was then used to calculate 100 models of OPA1 structure in the “open” conformation using the available crystal structures of human MxA [PDB code: 3SZR (doi:10.1016/j.immuni.2011.07.012)] and human DNM1L [PDB code: 4BEJ (doi:10.1038/emboj.2013.74)], using the Modeller 9.14 software (doi:10.1006/jmbi.1993.1626 P). The GDP molecule found in the human DNM1L structure was included in the modelling procedure. The best model was selected using the DOPE potential function built into Modeller (doi:10.1110/ps.062416606). A loop optimization routine was used to refine the regions that showed higher than average energy as calculated using the DOPE potential function. The final model was geometry optimized in the gas phase by using the UCSF Chimera (doi:10.1002/jcc.20084), the AMBER *ff14SB* force field (doi:10.1021/acs.jctc.5b00255), and the

AM1-BCC charges (doi:10.1002/jcc.10128). The stereochemical quality of the model structure was established using ProCheck (doi:10.1107/S0021889892009944). The results of this analysis confirm the reliability of the model structure.

The template structure used to calculate the OPA1 model structure in the “closed” conformation was prepared by dividing the model in the “open” conformations in two parts, one formed by the GTPase domain the other formed by the helical domain. The two parts of the OPA1 model in the “open” conformation was then superimposed to the corresponding domains of the known structure of the bacterial dynamin like protein from *Nostoc punctiforme* [PDB code: 2J68 (doi:10.1038/nature05312)]. This template structure was then used to calculate the model of OPA1 in the “closed” conformation, following the same protocol described above.

2.16. Reagents

Antibodies: DRP1, MFN1, MFN2 (Abnova); NDUFA9, UQCRC2, α subunits CV, actin (Abcam); COX IV, SDHA (ThermoFisher Scientific); OPA1 (BD Biosciences); tubulin (Sigma-Aldrich); VDAC (Biovision); horseradish peroxidase-conjugated secondary antibodies (Jackson ImmunoResearch or Alexafluor). ECL western blotting kit from Biorad or Thermo Scientific Pierce. The other reagents from Sigma-Aldrich.

3. RESULTS

3.1. Molecular and biochemical profile of fibroblasts bearing *OPA1* mutations

We have investigated fibroblasts derived from seven patients carrying four different *OPA1* missense mutations and five healthy donors. Three of these mutations were selected on the basis of their known clinical phenotypes, ranging from non-penetrant or very mild pure optic atrophy (I382M), to severe syndromic forms (G439V and R445H; see supplementary table 1 for description of patients' clinical phenotypes). The fourth mutation, D603H, clinically expressed as pure DOA with severe visual loss, is here reported and fully characterized for the first time (Supplementary table 1 for description of patients' clinical phenotypes). We have analyzed in detail these four mutations, intentionally including different clinical phenotypes (asymptomatic/mild optic atrophy, severe optic atrophy and syndromic optic atrophy), first in fibroblasts and then in other two cellular models generated "*ad hoc*".

The expression levels of MFN1, MFN2 and DRP1, the main proteins involved in the machinery of mitochondrial fusion and fission, were similar in control and DOA patients, whereas the amount of *OPA1* was reduced in fibroblasts with the I382M, R445H and D603H mutations and slightly increased in G439V fibroblasts (Fig. 1A-B). Sequencing of retro-transcribed *OPA1* mRNA in the same fibroblasts revealed the presence of both wild-type and mutated alleles (Fig. S1A), indicating that both the proteins were synthesized. Quantification of the relative amount of l- and s-forms revealed an increased l-/s-forms ratio for the G439V mutation only (Fig. 1C).

We then studied the energetic competence of DOA patients' fibroblasts, by evaluating initially the cellular ATP content during incubation in glucose-free DMEM containing galactose, a condition known to force cells to rely on OXPHOS for ATP synthesis. After 24h and 48h in DMEM-galactose, the ATP levels of controls markedly increased ($+60\pm 15\%$ and $+40\pm 17\%$, respectively), as a consequence of the shift from glycolytic to oxidative metabolism. Differently, all fibroblasts bearing *OPA1* mutations were unable to rise the ATP content, being the differences from controls statistically significant at 24h only, when cells have not yet adjusted their metabolism to the change

of carbohydrate source (Fig. 2A). The same trend was evident by expressing the ATP values as nmol/mg of protein (Fig. S1B). A similar behavior was previously reported for DOA fibroblasts harboring *OPA1* mutations leading to haploinsufficiency [24]. The oxygen consumption rate (OCR) was slightly reduced, without reaching statistical significance, in fibroblasts bearing the G439V mutation only (Fig. 2B-C), although the maximal/ATP-linked ratio and the respiratory control ratio (RCR) were similar in all cell lines (Fig. 2D-E). In DMEM-galactose the respiration was increased in all cell lines, but mutant fibroblasts were less efficient than controls, as evidenced by the non-significant reduction of OCR traces and maximal/ATP-linked ratio (Fig. 2F-H).

Semi-quantitative evaluation of the Complex I (CI) in gel activity (CI-IGA) and its densitometric analysis revealed that the amounts of isolated CI and of CI+III₂ supercomplex were reduced in mutated fibroblasts compared to controls, except for the D603H mutation. The level of the most abundant CI+III₂+IV supercomplex was similar to controls in all mutants, except for the D603H. The assembly of CV monomer was not compromised by any of the *OPA1* mutations (Fig. 2I-J). All together these results indicate that despite mutants' inability to increase the ATP content and respiration during the shift from glycolytic to oxidative metabolism, the supramolecular organization of OXPHOS complexes is not dramatically affected by *OPA1* mutations in fibroblasts. Considering the *OPA1* involvement in mtDNA maintenance [11,44], we also determined the mtDNA content. As reported in Fig. 3A, in fibroblasts with the I382M and D603H mutations the mtDNA copy number was similar to controls. Differently, the mtDNA amount was significantly reduced in R445H mutants and increased in fibroblasts with the G439V (Fig. 3A and Fig. S1C). The separate analysis of the two fibroblast cell lines carrying the R445H mutation revealed similar *OPA1* levels (Fig. S1D) but different mtDNA content (Fig. S1E). Indeed, only the fibroblasts derived from patient II exhibited a marked reduction of mtDNA copy number, as also confirmed by analysis in the muscle biopsy (Fig. S1F). The mtDNA amount in the muscle biopsy of the G439V patient was normal (Fig. S1F).

The mitochondrial network morphology was then investigated by fluorescence microscopy. Representative images of fibroblasts incubated in DMEM-glucose or DMEM-galactose are reported in Fig. 3B. Quantitative analysis of mitochondrial morphology of fibroblasts incubated in DMEM-glucose showed an almost complete filamentous mitochondrial network in controls and in cells with the I382M, whereas G439V and R445H mutations were associated with a slight increase of intermediate mitochondria. The D603H mutation presented a significant reduction of filamentous mitochondria and increase of intermediate mitochondria (Fig. 3C). In DMEM-galactose, the percentage of cells with fragmented mitochondria, which remained negligible in control fibroblasts, was variously increased by the presence of each *OPA1* mutation, being statistically significant for the G439V and R445H mutations (60% and 40%, respectively, Fig. 3D). Again, D603H mutation presented a significant reduction of filamentous mitochondria and an increase of intermediate mitochondria (Fig. 3C). The results are summarized in table 2.

All together these results underline the difficulty of studying the pathogenicity of an *OPA1* mutation and its molecular mechanism in patient fibroblasts that always present mild phenotypes, even when bearing severe mutations associated to DOA “plus”.

3.2. Molecular and biochemical profile of MEF bearing *OPA1* mutations

We took advantage of *Opal*^{-/-} MEFs to express the *OPA1* isoform 1 bearing each of the same four mutations analyzed in patients' fibroblasts. This cell model, previously characterized by our group [36], allows to examine the specific effect of each mutation in the same nuclear background and without the confounder of the wt allele.

Western blot analysis demonstrated that the balance of *OPA1* l- and s-forms compared to ISO1 as well as the level of the other mitochondrial shaping proteins was not influenced by the different mutations (Fig. 4A-B).

Because of the faster replication rate of MEFs compared to fibroblasts, the ATP content in DMEM-galactose was measured after 16h and 24h of incubation. After 16h, MEFs bearing the G439V and

R445H mutations exhibited a significant reduction of ATP levels, similar to those of *Opa1*^{-/-} MEFs, whereas MEFs with the other *OPA1* mutations were similar to wt (Fig. 4C and S2A). The OCR traces are reported in Fig. 4D. Variable respiratory deficits were apparent in *OPA1* mutated MEFs (Fig. 4D-E), ranging from a slight, not significant reduction of the maximal/ATP-linked respiration ratio apparent for I382M and D603H MEFs, to values similar to *Opa1*^{-/-} MEFs in R445H and G439V MEFs (Fig. F). These two mutations presented also a non-significant reduction of RCR (Fig. 4G), whereas all mutants, with the exception of I382M, showed a significant shift toward glycolysis, as indicated by decreased OCR/ECAR ratio (Fig. 4H).

The western blot analysis of OXPHOS subunits revealed reduced levels of NDUFA9 (CI), UQCRC2 (CIII) and COX IV (CIV) subunits in G439V and R445H MEFs (Fig. 5A-B).

Concordantly, the semi-quantitative evaluation of CI-IGA and its densitometric analysis showed a reduction of isolated CI, and CI+III₂ and CI+III₂+IV supercomplexes in G439V and R445H MEFs compared to wt or ISO1, whereas D603H and I382M mutant MEFs displayed almost normal supramolecular assembly. Noticeably, the band at higher molecular weight corresponding to the CI+III₂+IV_n supercomplex was almost absent in MEFs bearing mutations in the GTPase domain (Fig. 5C-D). Immunodetection of CV revealed in G439V and R445H MEFs, similarly to *Opa1*^{-/-} MEFs, a marked reduction of the band corresponding to the assembled monomer (F₁-F₀) and the appearance of two bands at lower molecular weight corresponding to free F₁, indicating the presence of partially disassembled CV sub-complexes (Fig. 5C). These results underline a severe energetic defect associated with G439V and R445H mutations, whereas D603H only induces a slight energetic dysfunction, completely absent in I382M cells.

It is noteworthy that the G439V and R445H mutations were associated with decreased mtDNA content, whereas the other two mutations exhibited values similar to those of wt and ISO1 MEFs (Fig. 6A).

Representative images of mitochondrial network of MEFs bearing *OPA1* mutations are reported in Fig. 6B. Quantification of network morphology showed that MEFs with the I382M mutation

presented a distribution similar to ISO1 MEFs, whereas the D603H induced both a significant increase in the percentage of cells with fragmented network and reduction of those with filamentous network. MEFs bearing the other two mutations exhibited the complete fragmentation of the mitochondrial network (Fig. 6C). The results are summarized in table 3.

Overall these results evidenced that I382M mutation, associated with asymptomatic/very mild DOA, did not perturb mitochondrial morphology and mtDNA content, whereas D603H mutation, linked to pure DOA with severe visual loss, promoted mitochondrial fragmentation without any mtDNA reduction. Finally, G439V and R445H mutations, related with DOA “plus”, induced both mitochondrial fragmentation and significant mtDNA content decrease.

To verify this emerging relationship between mtDNA and mitochondrial fragmentation as indicator of pure DOA or DOA “plus” outcome, we decided to examine three other mutations: R290Q (DOA “plus”; Supplementary table 1 for description of clinical phenotypes), S545R (pure DOA with severe optic atrophy [45] or DOA “plus” [11,31]) and Q785R (pure DOA [38]) (see positions within the OPA1 protein and other details in Table 1).

The expression of OPA1, MFN1, MFN2 and DRP1 proteins was not influenced by these three mutations (Fig. S2B). The mutation R290Q presented a significant decrease of mtDNA content ($-30 \pm 6\%$) and completely fragmented mitochondrial network (Fig S2C-E), whereas the S545R mutation exhibited a non-significant decline ($-25 \pm 10\%$) in presence of complete mitochondrial fragmentation (Fig S2C-E). The Q785R mutation did not change the mtDNA amount, still presenting a substantial increase in the percentage of cells with fragmented network ($+60 \pm 4\%$) (Fig S2C-E). Thus, the Q785R mutation acts as the D603H, both associated to pure DOA, the R290Q behaves as the DOA “plus” related G439V and R445H mutations, and the S545R has an borderline behavior between pure DOA with severe optic atrophy and DOA “plus”.

3.3. Phenotypic profile of yeast strain harboring mutations in *OPA1*

The yeast *S. cerevisiae* has been extensively used as an *in vivo* model to study and validate the pathogenicity of mutations in genes involved in mitochondrial diseases, thanks to its ability to grow in absence of OXPHOS activity. Although yeast Mgm1 and OPA1 are orthologous, the sequence of the two proteins is poorly conserved, and the whole OPA1 cannot complement the deletion of *MGM1* [32].

In order to validate *OPA1* mutations in non-conserved residues, we have previously generated an *MGM1/OPA1* chimeric construct (called *CHIM3*), encoding a protein composed of the N-terminal region of Mgm1, comprising the sequence required for mitochondrial import, and the transmembrane domain, fused to the catalytic region of OPA1, containing the GTPase, the middle and the GED domains [32].

To acquire further insights on the consequences of the four missense mutations studied in fibroblasts and in MEFs on the OXPHOS phenotype, we exploited the *CHIM3* allele. Two of the four mutations studied in fibroblasts and MEF models (I382M and R445H) were previously described in our system [32], and here re-analyzed adding the further G439V and D603H mutations.

At first, the *chim3* mutant alleles, obtained through mutagenic PCR, were introduced in the yeast centromeric (single copy) plasmid pFL39TEToff, under the strong yeast promoter *CYCI* fused with seven repeats of the *tetO* operator cassettes. Since deletion of *MGM1* makes the strain irreversibly devoid of mtDNA, *CHIM3* alleles were introduced in the haploid W303-1B Δ *mgm1* strain transformed with the plasmid pFL38*MGM1*, which was subsequently lost by the plasmid shuffling technique in order to obtain a strain expressing only the *CHIM3* alleles. The ability of the mutant alleles to complement the oxidative growth defect of the *mgm1* Δ strain was then evaluated by phenotypic analysis in medium supplemented with a non-fermentable carbon source and glucose as the control. All mutant strains, except the one harboring the I382M mutation, showed a respiratory deficient phenotype, confirming the severe pathological role of these mutations (Fig. 7A).

CHIM3^{I382M} strain showed a slightly decreased growth (Fig. 7A) and reduction of respiratory

activity as well as of respiratory complexes activities [32], confirming its nature of hypomorphic allele. Furthermore, no mtDNA was present in each of the mutant strain, as determined by qPCR, except for the strain harboring the I382M mutation, for which a 20% decrease of mtDNA levels was observed ($p < 0,05$ in a two-tailed t test) [32]. Western blot analysis showed that in all the mutant strains the total level of Chim3 was grossly similar, but all strains, except those carrying the I382M mutation, presented an unbalanced ratio of the l- and s-forms, with reduced amount of the s-forms compared to the *CHIM3* wt strain, suggesting that the l-forms are not correctly processed (Fig. 7B and 7C). Finally, we observed the mitochondrial morphology of wt and mutant strains previously transformed with a plasmid harboring a GFP isoform localizing to mitochondria. As previously reported [32], we distinguished three major kinds of mitochondrial morphology: filamentous, fragmented and giant mitochondria (Fig. 7D). For each strain, we measured the percentage of cells harboring each of the three morphologies. We found that 35% of the *CHIM3* cells had a filamentous morphology, whereas in the remaining cells mitochondria were fragmented or collapsed to form giant mitochondria. In the I382M strain, only the 20% of cells had filamentous mitochondria, whereas in all the other strains, including those transformed with the empty plasmid, all respiratory deficient, no cells with a filamentous morphology were observed (Fig. 7E).

To test the dominance/recessivity of the mutations, diploid strains have been created. The diploid strain DW1.1/pFL38MGM1-pFL36TEToffCHIM3, deleted in both copies of genomic *MGM1* and transformed with a plasmid copy of *MGM1* and a plasmid copy of wt *CHIM3*, was transformed with the *CHIM3* alleles cloned in pFL36TEToff. *MGM1* was then lost by plasmid shuffling. The final strains contained either two copies of wild type *CHIM3* (homoallelic diploid), a *CHIM3* allele plus an empty plasmid (hemiallelic diploid) or a wild type *CHIM3* and a mutated *chim3* mutant copy (heteroallelic diploid). The growth phenotype of the diploid strains was evaluated by spot assay analysis on oxidative carbon sources (Fig. 7F). The growth of the heteroallelic strain containing the I382M mutation was similar to that of the homoallelic and hemiallelic strains. In all the remaining heteroallelic strains the growth was affected compared to the homoallelic one,

although at different extents, indicating that the mutations are dominant. In particular, R445H and D603H mutations strongly decreased the oxidative growth when in heterozygosis with *CHIM3*. Concordantly, the respiratory activity of heteroallelic strains carrying the mutations was reduced for all strains except for that bearing I382M mutation (Fig. 7G), similar to the results of growth analysis. Finally, strains harboring G439V, R445H and D603G showed a significant decrease of cells with filamentous mitochondrial morphology, being again the strains R445H and D603G more affected (Fig. 7H). The results are summarized in table 4.

3.4. Phenotypic profile of yeast strain harboring additional mutations in *OPA1*

Thanks to the flexibility of yeast in studying mutations in *OPA1*, here we have also investigated other seven substitutions found in patients with both DOA or DOA “plus” phenotype and localized in the different *OPA1* domains (see positions within the *OPA1* protein and other details in Table 1). Concerning the haploid strains, we found that: (i) in all mutants, the oxidative growth was absent (Fig. 8A); (ii) no mtDNA was present, as measured with qPCR; (iii) the ratio of the l- and s-forms was unbalanced, although at different extent, except for strain harboring Q785R and V910D mutation (Fig. 8B and 8C); (iv) no filamentous mitochondrial morphology was observed (Fig. 8D). Regarding the diploid strains, we found that most of the heteroallelic strains displayed a decreased oxidative growth, which was almost absent for strain harboring L593P mutation (Fig. 8E). On the contrary, in heteroallelic strains containing the Q785R and V910D mutations the growth was similar to that of the homoallelic one. The respiratory activity (Fig. 8F) and the mitochondrial morphology (Fig. 8G) were grossly congruent with the oxidative growth phenotype, suggesting that all the mutations, except the Q785R and the V910D ones, behaved as dominant negative. To ascertain whether these results were not influenced by the use of a chimeric gene, the S298N and I382M mutations, which involve conserved residues, were introduced at the corresponding position S241N and I322M in yeast *Mgm1*. The *mgm1* haploid strain carrying the S241N mutation was unable to grow on respiratory carbon sources (data not shown), as observed for the chimeric

strain with the equivalent mutation (Fig. 3A), but not for the I322M mutation, as previously reported [32]. In heteroallelic condition, the *mgm1*^{S241N} allele behaved as dominant negative, with decreased oxidative growth and respiratory activity compared to both homoallelic (*MGM1/MGM1*) and hemiallelic (*MGM1*/empty plasmid) strains. On the contrary, heteroallelic strain harboring *mgm1*^{I322M}, corresponding to the human mutation I382M, behaved as the homoallelic strain (Fig. S3A-B).

3.5. OPA1 structural model and mutations mapping

The structural determinants associated with the *OPA1* mutations were analyzed through the calculations of structural models of OPA1. A homology model of human OPA1 was previously inferred on the basis of a distant homologue from the bacteria *Nostoc punctiforme* [11]. The recent release in the Protein Data Bank (PDB) of the structures of several OPA1 eukaryotic homologues, prompted us to develop a new OPA1 model. In particular, the new crystal structures feature the helical domain in a completely different conformation with respect to the GTPase domain, resulting in an elongated conformation (“open” conformation hereafter). We, thus, speculate that the bacterial OPA1 homologue from *N. punctiforme* structure shows the helical domain in a “close” conformation. Fig. 9A reports the homology models obtained for human OPA1 in the “open” and in the “close” conformations.

The *OPA1* mutations were mapped on the new structural models (Fig. 9B). The I382M and G439V are located near the G1 and G3 loops involved in the GTP binding and/or hydrolysis, conversely the R445H is positioned on the surface of the GTPase domain, in a region coming in contact with the helical domain in the “close” conformation, where it might impair the “closing” movement. The novel D603H sits in the “hinge” between the GTPase and the helical domains. An analogous structural mapping was performed for the other mutations analyzed in MEFs and in the yeast *MGM1/OPA1* chimera: the R290Q, located in the first β -strand of the dynamin-type G domain, may impair the H-bond network or, more in general, the packing of this region. The S298N and

G300E mutations are in the G1 loop, the T499P is in contact with G1 loop and the S545R is in the GTP binding site. All these latter five mutations might alter GTP binding. The L593P and V910D mutations are located in the hinge of the two domains and, as D603H, may interfere with the helical domain motion. Finally, the Q785R mutation is positioned in the most external part of the helical domain, possibly hindering the interaction with another OPA1 protein during dimerization.

ACCEPTED MANUSCRIPT

4. DISCUSSION

This study provides the detailed characterization of the pathological consequences generated by a series of *OPA1* mutations associated with a variety of clinical phenotypes, taking advantage of two novel cell models generated *ad hoc* to evaluate cellular dysfunctions strictly dependent on *OPA1* mutations: MEFs and yeasts. These models display a clear-cut phenotype that provides, by complementary information, a quick definition of mutation's pathogenicity, thus proving useful for patient's diagnosis. Strikingly, some mutant alleles literally behave as null mutations (G439V, R445H and R290Q), when unopposed by the co-presence of the wt allele in MEFs, whereas at the opposite end a hypomorphic mutation such as I382M reveals only a slight damaging potential.

4.1. Fibroblast model

Fibroblasts from DOA patients are the commonest cell model used to date to analyze the effect of different *OPA1* mutations, but suffer numerous limitations, such as great heterogeneity of phenotypes due to the individual nuclear and mitochondrial genomes variability and the presence of the wt allele. Furthermore, fibroblasts fail to display the features typically seen only in post-mitotic tissues, relevantly the mtDNA alterations (depletion/deletions). On the other hand, the experimental use of muscle tissue derived from patient's biopsies is limited by the invasiveness of the procedure and the small amounts of material. Different degrees of energetic dysfunction, mitochondrial morphology and *cristae* alteration have been reported in DOA fibroblasts [11,21,23,24,30,46], particularly after enhancing the phenotype by metabolic stress conditions (DMEM-galactose) [24,30]. Furthermore, generation of primary fibroblast cultures takes a relatively long time and these cells suffer the disadvantage of a finite life span, undergoing replicative senescence.

In this study the mtDNA content, energetics and network morphology were assessed in fibroblasts bearing three well know *OPA1* mutations (I382M, G439V and R445H) and one new mutation (D603H). Remarkably, the G439V and R445H mutations, associated with a similarly severe clinical phenotype, induced a substantial and opposite alteration in the mtDNA amount, a previously unrecognized feature in fibroblasts. The analysis of patient's muscle bearing the G439V

mutation confirmed our previously reported result of an mtDNA content similar to controls [11]. Interestingly, for the R445H mutation, only the fibroblasts and corresponding muscle biopsy from patient II presented mtDNA depletion, whereas a normal amount of mtDNA was observed for patient I, notwithstanding the same reduction in OPA1 level in both cases. This observation suggests that other modifying factors might be influential. For example, considering the father-daughter segregation of the R445H mutation, the mtDNA haplogroup differs, as well as other unknown nuclear variants, the age and gender. Considering the limited number of patients explored in this study, an appropriate large-scale investigation on this issue is warranted. From the energetic point of view, the mutations did not significantly influence the supercomplexes assembly, although a general and significant decrease in cellular ATP levels and respiration was detected after metabolic stress. In glucose, the basal and maximal mitochondrial respirations were slightly but not significantly reduced only with the G439V mutation, however both respiratory ratios were unaffected. Thus, although some energetic impairment was observed only after metabolic stress, a specific correlation with the mutation type could not be clearly identified. The only parameter that almost linearly correlated with the severity of patients' clinical phenotype was the mitochondrial morphology in DMEM-galactose. As summarized in Table 2, the overall evaluation of the five readouts shows that each mutation presents one, two or three dysfunctional parameters, not linearly correlated with the patient's clinical conditions.

4.2. MEFs model

As a second model, the MEF lines stably expressing isoform 1 have proved also extremely useful, since the quick and easy insertion of the *OPA1* missense mutations allowed for a detailed biochemical investigation of the dysfunctional phenotypes, which were enhanced as compared to fibroblasts and nicely correlated with the clinical severity observed in the patients. In fact, both G439V and R445H mutations induced drastic mtDNA depletion, impaired respiration, remarkable supercomplexes disorganization and complete mitochondrial network fragmentation, which are all in excellent agreement with the clinical severity of these DOA “plus” patients. The same

phenotypes were observed also for the R290Q and the G300E mutations [36], both associated with DOA “plus”. Opposite, the I382M mutation did not exhibit any significant dysfunction, except for its tendency to reduced respiration, in agreement with its role of mildly pathogenic or hypomorphic mutation. Interestingly, the novel D603H mutation, despite maintaining a normal mtDNA and ATP content, showed a slightly reduced respiration, a mild CV disassembly and a significant increase in mitochondrial network fragmentation, again in agreement with the intermediate clinical phenotype of these patients with pure DOA and severe visual dysfunction. Thus, as summarized in table 3, in MEFs model the number of defective hallmarks linearly increased with the severity of clinical phenotype of the mutation, being only one affected for the I382M mutation, three for the D603H mutation and five for the G439V and R445H mutations. While the Q785R mutation presented normal mtDNA and partially affected mitochondrial morphology, similar to the D603H mutation, the S545R mutation had an intermediate behavior, borderline across phenotypes. Indeed, the complete fragmentation of the mitochondrial network was associated with only a slight, non-significant reduction of mtDNA amount, supporting a borderline nature of this variant, causing either DOA or DOA “plus” possibly depending on modulation of other genetic and/or environmental modifiers. MEFs analysis suggests that a complete fragmentation of the mitochondrial network, in association with mtDNA depletion, hallmarks the DOA “plus” phenotype, whereas if these two parameters are mildly affected the final outcome is expected to be pure DOA. This hypothesis is represented in the scheme of figure 10.

4.3. Yeast model

Switching to the yeast model, by using a chimeric gene, the greatest advantage was the insight on the genetic mechanism of *OPAI* mutations and the kind of dominance of the mutations. In fact, *CHIM3* homoallelic and hemiallelic strains showed no difference in the respiratory phenotype, contrary to humans, likely due to a stronger promoter of the *CHIM3* allele, which guarantees a sufficient, but not toxic, expression in the diploid strain too. However, the comparison of the haploid and diploid models may discern three types of mutant alleles. (i) If the haploid strain shows

a partially defective respiratory phenotype, i.e. a reduced oxidative growth and/or a reduced respiratory activity, and the heteroallelic strain behaves as the homo- and hemiallelic ones, then the mutant allele can be considered hypomorphic, as observed for I382M mutation. (ii) If the haploid strain displays no oxidative phenotype, i.e. is unable to grow on oxidative carbon sources, and the heteroallelic strain behaves as the hemiallelic one, then the mutant allele can be considered null, since it does not interfere with the activity of the wt allele. (iii) If the haploid strain displays no oxidative phenotype and the heteroallelic strain shows a decreased oxidative growth compared to the hemiallelic, the mutant allele can be considered antimorphic, resulting in a dominant negative phenotype.

The current and our previous study [32] clearly revealed that all mutations associated with DOA or DOA “plus” phenotype cause, in haploid strain, the inability to grow on oxidative carbon sources due to loss of mtDNA. The only exception is the I382M, which is either associated with a very mild phenotype [47] or it has been proposed to act as a hypomorphic allele [16,19].

While human *OPA1* nonsense mutations are associated in most cases with non-syndromic DOA due to haploinsufficiency as a genetic mechanism, missense mutations can be associated with both pure DOA or DOA “plus”, due to either haploinsufficiency or negative dominance, depending on the mutation [13,48]. Yeast analysis revealed that most mutations, with the exception of two, behave as partially dominant due to a negative dominance. The reduced oxidative growth and respiratory activity of heteroallelic strain suggest that the mutant isoform interferes with the wt protein. This result suggests two scenarios: (i) most of the missense mutations found in humans are *per se* partially dominant negative, and the severity of the phenotype as defined by pure DOA or DOA “plus”, depends on the degree of interference of the mutant protein on wt in affecting mtDNA maintenance and mitochondrial fragmentation. In addition, some missense mutations may adjunctively impinge on the stability of the mutant protein itself. (ii) Alternatively, most mutations are dominant and have the potential to cause a DOA “plus” phenotype, and the severity of disease depends on other factors, such as the co-presence of modifying variants in other genes, as well as

environmental factors or age/gender of the patients. This is the case for the S545R mutation, which was found associated with either DOA or DOA “plus” in different patients [13,31,45].

Intriguingly, we noticed that most mutations, including all the dominant negative ones, altered the relative amount of the l- and s-forms in the mutant haploid yeast strains compared with the wt, suggesting that such mutations can also impair the protein processing. In all cases, the levels of the s-form are decreased and, thus, the ratio of l- and s-forms is increased. By using both *Opa1* null MEFs expressing different combination of *OPA1* isoforms and *OPA1* silenced HeLa cells, we have previously demonstrated that increased l- to s-forms ratio is associated with a highly fragmented mitochondrial network [36]. A similar phenotype was previously reported in yeast, where overexpression of the *Mgm1* l-form, increasing the l- to s-forms ratio, lead to both loss of mtDNA and fragmentation of mitochondrial network [49]. Thus, increased l-/s-forms ratio in yeast could be used as an additional indicator of pathogenicity of the mutations.

4.4. Models comparison

The comparison of fibroblast and MEF results raises two observations deserving some further comments. First, there is a remarkable discrepancy in terms of *OPA1* protein abundance, which is partially reduced in fibroblasts carrying the I382M, R445H and D603H mutations, whereas this is not affected in MEFs expressing the single mutant allele on isoform 1. The reduced amount of *OPA1* protein was already noticed in other studies [15,50]. We envisage a possible explanation by hypothesizing that the interaction between mutant and wt protein may perturb *OPA1* oligomers stability, favoring degradation. Second, we noticed that in patient’s derived fibroblasts CV and CI-containing supercomplexes were properly assembled, at difference with MEFs carrying the most severe mutant mutations. We also determined a normal supramolecular organization in fibroblasts carrying *OPA1* mutation causing haploinsufficiency mutations (Del Dotto and Zanna, unpublished results). These observations challenge the previously proposed relevance of supercomplex assembly as driving mechanism for the bioenergetics deficiency in DOA [51]. Considering that MEFs expressing the most severe *OPA1* missense mutations displayed a significant perturbation of

supercomplexes organization, there must be a sufficient complementation by the wt allele overcoming this potentially harmful mechanism in patient's fibroblasts. This conundrum deserves further investigations.

In yeast model most *OPA1* mutations strongly compromise mtDNA content, mitochondrial morphology, oxidative growth and energetics, making difficult to identify the degrees of severity related to the different mutations. However, thanks to the chimeric gene, yeast modeling is excellent to determining whether a mutation is pathogenic or not and to evaluating its dominance/recessivity. Conversely, the MEFs model nicely defines the biochemical features, highlighting also different degrees of severity associated with the mutations, but does not inform on dominance/recessivity. These two models are therefore complementary, operating in parallel to uncover DOA pathophysiology.

A further comparison of MEFs and haploid yeast strains showed that: (i) in both models, the mutant alleles bearing G439V and R445H mutations behaved as a null allele concerning mtDNA content, mitochondrial morphology and respiratory activity; (ii) MEF with I382M showed only a slightly altered phenotype, whereas yeast showed a slight but statistically significant alterations of mtDNA levels and mitochondrial morphology; (iii) for the other mutations, which behaved as null in the yeast model, there was a partial overlap with the phenotype found in MEFs, since the S545R mutation caused a complete mitochondrial fragmentation associated with a slight decrease of mtDNA levels, whereas D603H and Q785R mutations caused substantial increase in cells with fragmented network and, for the former mutation, a decrease of the OCR/ECAR ratio.

Finally, the accurate mapping of all *OPA1* mutations in the new *OPA1* structural model showed that all mutations localized in the GTPase domain and involved in GTP binding/hydrolysis or GDP release may cause DOA or DOA "plus". Interestingly, the mutations L593P, D603H and V910D, which appear harmless in the "open" conformation, reveal their detrimental potential only when considered in the "close" conformation, being located in the hinge of the two domains, thus interfering with the helical domain motion.

5. Conclusion

In conclusion, our current results strongly support the combined analysis of human, MEF and yeast cell models for “deep phenotyping” of *OPAI* mutations and comprehensive dissection of their mechanistic effects. These cell models hold great promises to developing new therapeutic interventions, taking advantage of the yeast model for powerful high throughput screening of molecules, whose efficiency could be then further validated in the mouse and human cell models.

ACCEPTED MANUSCRIPT

ACKNOWLEDGEMENTS

This work was supported by the Futuro in Ricerca FIR2013 from the Ministero della Istruzione Università e Ricerca (MIUR) [RBFR131WDS-001 to CZ and RBFR131WDS-002 to EB]; and the National Institutes of Health [GM110039 to DCC]. We thank Mirca Lazzaretti for the helpful technical assistance with the fluorescence microscope in yeast.

CONFLICTS OF INTEREST STATEMENT

The authors declare no financial conflict of interest that might be construed to influence the results or interpretation of the manuscript.

AUTHORS CONTRIBUTIONS

Conceptualization, VDD, EB and CZ; Methodology, VDD, EB and CZ; Investigation, VDD, MF, FM, AM, SJA, LC, CLM, CN, EB and CZ; Resources, DC; Writing – Original Draft, VDD, EB and CZ; Writing – Review & Editing, VDD, TL, PG, DC, VC, MR, EB and CZ; Visualization, VDD, EB and CZ; Funding Acquisition, DC and CZ; Supervision, MR, TL, PG, EB and CZ; Project Administration, EB and CZ.

REFERENCES

- [1] P. Kjer, Infantile optic atrophy with dominant mode of inheritance: a clinical and genetic study of 19 Danish families, *Acta Ophthalmol. Suppl.* 164 (1959) 1–147.
- [2] G. Lenaers, C. Hamel, C. Delettre, P. Amati-Bonneau, V. Procaccio, D. Bonneau, P. Reynier, D. Milea, Dominant optic atrophy, *Orphanet J. Rare Dis.* 7 (2012) 46. doi:10.1186/1750-1172-7-46.
- [3] C. Delettre, G. Lenaers, J.M. Griffoin, N. Gigarel, C. Lorenzo, P. Belenguer, L. Pelloquin, J. Grosgeorge, C. Turc-Carel, E. Perret, C. Astarie-Dequeker, L. Lasquellec, B. Arnaud, B. Ducommun, J. Kaplan, C.P. Hamel, Nuclear gene OPA1, encoding a mitochondrial dynamin-related protein, is mutated in dominant optic atrophy, *Nat. Genet.* 26 (2000) 207–210. doi:10.1038/79936.
- [4] C. Alexander, M. Votruba, U.E. Pesch, D.L. Thiselton, S. Mayer, A. Moore, M. Rodriguez, U. Kellner, B. Leo-Kottler, G. Auburger, S.S. Bhattacharya, B. Wissinger, OPA1, encoding a dynamin-related GTPase, is mutated in autosomal dominant optic atrophy linked to chromosome 3q28, *Nat. Genet.* 26 (2000) 211–215. doi:10.1038/79944.
- [5] A. Olichon, L.J. Emorine, E. Descoins, L. Pelloquin, L. Brichese, N. Gas, E. Guillou, C. Delettre, A. Valette, C.P. Hamel, B. Ducommun, G. Lenaers, P. Belenguer, The human dynamin-related protein OPA1 is anchored to the mitochondrial inner membrane facing the inter-membrane space, *FEBS Lett.* 523 (2002) 171–176.
- [6] T. MacVicar, T. Langer, OPA1 processing in cell death and disease - the long and short of it, *J. Cell Sci.* 129 (2016) 2297–2306. doi:10.1242/jcs.159186.
- [7] Z. Song, H. Chen, M. Fiket, C. Alexander, D.C. Chan, OPA1 processing controls mitochondrial fusion and is regulated by mRNA splicing, membrane potential, and Yme1L, *J. Cell Biol.* 178 (2007) 749–755. doi:10.1083/jcb.200704110.
- [8] V. Del Dotto, M. Fogazza, V. Carelli, M. Rugolo, C. Zanna, Eight human OPA1 isoforms, long and short: What are they for?, *Biochim. Biophys. Acta BBA - Bioenerg.* 1859 (2018) 263–269.

doi:10.1016/j.bbabbio.2018.01.005.

[9] M. Ferré, A. Caignard, D. Milea, S. Leruez, J. Cassereau, A. Chevrollier, P. Amati-Bonneau, C. Verny, D. Bonneau, V. Procaccio, P. Reynier, Improved locus-specific database for OPA1 mutations allows inclusion of advanced clinical data, *Hum. Mutat.* 36 (2015) 20–25.

doi:10.1002/humu.22703.

[10] P. Amati-Bonneau, D. Milea, D. Bonneau, A. Chevrollier, M. Ferré, V. Guillet, N. Gueguen, D. Loiseau, M.-A.P. de Crescenzo, C. Verny, V. Procaccio, G. Lenaers, P. Reynier, OPA1-associated disorders: phenotypes and pathophysiology, *Int. J. Biochem. Cell Biol.* 41 (2009) 1855–1865. doi:10.1016/j.biocel.2009.04.012.

[11] P. Amati-Bonneau, M.L. Valentino, P. Reynier, M.E. Gallardo, B. Bornstein, A. Boissière, Y. Campos, H. Rivera, J.G. de la Aleja, R. Carroccia, L. Iommarini, P. Labauge, D. Figarella-Branger, P. Marcorelles, A. Furby, K. Beauvais, F. Letournel, R. Liguori, C. La Morgia, P. Montagna, M. Liguori, C. Zanna, M. Rugolo, A. Cossarizza, B. Wissinger, C. Verny, R. Schwarzenbacher, M.A. Martín, J. Arenas, C. Ayuso, R. Garesse, G. Lenaers, D. Bonneau, V. Carelli, OPA1 mutations induce mitochondrial DNA instability and optic atrophy “plus” phenotypes, *Brain J. Neurol.* 131 (2008) 338–351. doi:10.1093/brain/awm298.

[12] P. Yu-Wai-Man, P.G. Griffiths, A. Burke, P.W. Sellar, M.P. Clarke, L. Gnanaraj, D. Ah-Kine, G. Hudson, B. Czermin, R.W. Taylor, R. Horvath, P.F. Chinnery, The prevalence and natural history of dominant optic atrophy due to OPA1 mutations, *Ophthalmology.* 117 (2010) 1538–1546, 1546.e1. doi:10.1016/j.ophtha.2009.12.038.

[13] P. Yu-Wai-Man, P.G. Griffiths, G.S. Gorman, C.M. Lourenco, A.F. Wright, M. Auer-Grumbach, A. Toscano, O. Musumeci, M.L. Valentino, L. Caporali, C. Lamperti, C.M. Tallaksen, P. Duffey, J. Miller, R.G. Whittaker, M.R. Baker, M.J. Jackson, M.P. Clarke, B. Dhillon, B. Czermin, J.D. Stewart, G. Hudson, P. Reynier, D. Bonneau, W. Marques, G. Lenaers, R. McFarland, R.W. Taylor, D.M. Turnbull, M. Votruba, M. Zeviani, V. Carelli, L.A. Bindoff, R. Horvath, P. Amati-Bonneau, P.F. Chinnery, Multi-system neurological disease is common in

patients with OPA1 mutations, *Brain J. Neurol.* 133 (2010) 771–786. doi:10.1093/brain/awq007.

[14] P. Yu-Wai-Man, A. Spyropoulos, H.J. Duncan, J.V. Guadagno, P.F. Chinnery, A multiple sclerosis-like disorder in patients with OPA1 mutations, *Ann. Clin. Transl. Neurol.* 3 (2016) 723–729. doi:10.1002/acn3.323.

[15] V. Carelli, O. Musumeci, L. Caporali, C. Zanna, C. La Morgia, V. Del Dotto, A.M. Porcelli, M. Rugolo, M.L. Valentino, L. Iommarini, A. Maresca, P. Barboni, M. Carbonelli, C. Trombetta, E.M. Valente, S. Patergnani, C. Giorgi, P. Pinton, G. Rizzo, C. Tonon, R. Lodi, P. Avoni, R. Liguori, A. Baruzzi, A. Toscano, M. Zeviani, Syndromic parkinsonism and dementia associated with OPA1 missense mutations, *Ann. Neurol.* 78 (2015) 21–38. doi:10.1002/ana.24410.

[16] V. Carelli, M. Sabatelli, R. Carrozzo, T. Rizza, S. Schimpf, B. Wissinger, C. Zanna, M. Rugolo, C. La Morgia, L. Caporali, M. Carbonelli, P. Barboni, C. Tonon, R. Lodi, E. Bertini, “Behr syndrome” with OPA1 compound heterozygote mutations, *Brain J. Neurol.* 138 (2015) e321. doi:10.1093/brain/awu234.

[17] A. Nasca, T. Rizza, M. Doimo, A. Legati, A. Ciolfi, D. Diodato, C. Calderan, G. Carrara, E. Lamantea, C. Aiello, M. Di Nottia, M. Niceta, C. Lamperti, A. Ardisson, S. Bianchi-Marzoli, G. Iarossi, E. Bertini, I. Moroni, M. Tartaglia, L. Salviati, R. Carrozzo, D. Ghezzi, Not only dominant, not only optic atrophy: expanding the clinical spectrum associated with OPA1 mutations, *Orphanet J. Rare Dis.* 12 (2017) 89. doi:10.1186/s13023-017-0641-1.

[18] R. Spiegel, A. Saada, P.J. Flannery, F. Burté, D. Soiferman, M. Khayat, V. Eisner, E. Vladovski, R.W. Taylor, L.A. Bindoff, A. Shaag, H. Mandel, O. Schuler-Furman, S.A. Shalev, O. Elpeleg, P. Yu-Wai-Man, Fatal infantile mitochondrial encephalomyopathy, hypertrophic cardiomyopathy and optic atrophy associated with a homozygous OPA1 mutation, *J. Med. Genet.* 53 (2016) 127–131. doi:10.1136/jmedgenet-2015-103361.

[19] T. Bonifert, K.N. Karle, F. Tonagel, M. Batra, C. Wilhelm, Y. Theurer, C. Schoenfeld, T. Kluba, Y. Kamenisch, V. Carelli, J. Wolf, M.A. Gonzalez, F. Speziani, R. Schüle, S. Züchner, L. Schöls, B. Wissinger, M. Synofzik, Pure and syndromic optic atrophy explained by deep intronic

OPA1 mutations and an intralocus modifier, *Brain J. Neurol.* 137 (2014) 2164–2177.

doi:10.1093/brain/awu165.

[20] V. Del Dotto, M. Fogazza, G. Lenaers, M. Rugolo, V. Carelli, C. Zanna, OPA1: How much do we know to approach therapy?, *Pharmacol. Res.* 131 (2018) 199–210.

doi:10.1016/j.phrs.2018.02.018.

[21] P. Amati-Bonneau, A. Guichet, A. Olichon, A. Chevrollier, F. Viala, S. Miot, C. Ayuso, S. Odent, C. Arrouet, C. Verny, M.-N. Calmels, G. Simard, P. Belenguer, J. Wang, J.-L. Puel, C. Hamel, Y. Malthièry, D. Bonneau, G. Lenaers, P. Reynier, OPA1 R445H mutation in optic atrophy associated with sensorineural deafness, *Ann. Neurol.* 58 (2005) 958–963. doi:10.1002/ana.20681.

[22] A. Olichon, T. Landes, L. Arnauné-Pelloquin, L.J. Emorine, V. Mils, A. Guichet, C. Delettre, C. Hamel, P. Amati-Bonneau, D. Bonneau, P. Reynier, G. Lenaers, P. Belenguer, Effects of OPA1 mutations on mitochondrial morphology and apoptosis: relevance to ADOA pathogenesis, *J. Cell. Physiol.* 211 (2007) 423–430. doi:10.1002/jcp.20950.

[23] A. Chevrollier, V. Guillet, D. Loiseau, N. Gueguen, M.-A.P. de Crescenzo, C. Verny, M. Ferre, H. Dollfus, S. Odent, D. Milea, C. Goizet, P. Amati-Bonneau, V. Procaccio, D. Bonneau, P. Reynier, Hereditary optic neuropathies share a common mitochondrial coupling defect, *Ann. Neurol.* 63 (2008) 794–798. doi:10.1002/ana.21385.

[24] C. Zanna, A. Ghelli, A.M. Porcelli, M. Karbowski, R.J. Youle, S. Schimpf, B. Wissinger, M. Pinti, A. Cossarizza, S. Vidoni, M.L. Valentino, M. Rugolo, V. Carelli, OPA1 mutations associated with dominant optic atrophy impair oxidative phosphorylation and mitochondrial fusion, *Brain J. Neurol.* 131 (2008) 352–367. doi:10.1093/brain/awm335.

[25] M.V. Alavi, S. Bette, S. Schimpf, F. Schuettauf, U. Schraermeyer, H.F. Wehrl, L. Ruttiger, S.C. Beck, F. Tonagel, B.J. Pichler, M. Knipper, T. Peters, J. Laufs, B. Wissinger, A splice site mutation in the murine *OPA1* gene features pathology of autosomal dominant optic atrophy, *Brain J. Neurol.* 130 (2007) 1029–1042. doi:10.1093/brain/awm005.

[26] V.J. Davies, A.J. Hollins, M.J. Piechota, W. Yip, J.R. Davies, K.E. White, P.P. Nicols, M.E.

- Boulton, M. Votruba, Opa1 deficiency in a mouse model of autosomal dominant optic atrophy impairs mitochondrial morphology, optic nerve structure and visual function, *Hum. Mol. Genet.* 16 (2007) 1307–1318. doi:10.1093/hmg/ddm079.
- [27] P.A. Williams, J.E. Morgan, M. Votruba, Mouse models of dominant optic atrophy: what do they tell us about the pathophysiology of visual loss?, *Vision Res.* 51 (2011) 229–234. doi:10.1016/j.visres.2010.08.031.
- [28] R. Lodi, C. Tonon, M.L. Valentino, D. Manners, C. Testa, E. Malucelli, C. La Morgia, P. Barboni, M. Carbonelli, S. Schimpf, B. Wissinger, M. Zeviani, A. Baruzzi, R. Liguori, B. Barbiroli, V. Carelli, Defective mitochondrial adenosine triphosphate production in skeletal muscle from patients with dominant optic atrophy due to OPA1 mutations, *Arch. Neurol.* 68 (2011) 67–73. doi:10.1001/archneurol.2010.228.
- [29] P. Yu-Wai-Man, M.I. Trenell, K.G. Hollingsworth, P.G. Griffiths, P.F. Chinnery, OPA1 mutations impair mitochondrial function in both pure and complicated dominant optic atrophy, *Brain J. Neurol.* 134 (2011) e164. doi:10.1093/brain/awq288.
- [30] V. Agier, P. Oliviero, J. Lainé, C. L’Hermitte-Stead, S. Girard, S. Fillaut, C. Jardel, F. Bouillaud, A.L. Bulteau, A. Lombès, Defective mitochondrial fusion, altered respiratory function, and distorted cristae structure in skin fibroblasts with heterozygous OPA1 mutations, *Biochim. Biophys. Acta.* 1822 (2012) 1570–1580. doi:10.1016/j.bbadis.2012.07.002.
- [31] G. Hudson, P. Amati-Bonneau, E.L. Blakely, J.D. Stewart, L. He, A.M. Schaefer, P.G. Griffiths, K. Ahlqvist, A. Suomalainen, P. Reynier, R. McFarland, D.M. Turnbull, P.F. Chinnery, R.W. Taylor, Mutation of OPA1 causes dominant optic atrophy with external ophthalmoplegia, ataxia, deafness and multiple mitochondrial DNA deletions: a novel disorder of mtDNA maintenance, *Brain J. Neurol.* 131 (2008) 329–337. doi:10.1093/brain/awm272.
- [32] C. Nolli, P. Goffrini, M. Lazzaretti, C. Zanna, R. Vitale, T. Lodi, E. Baruffini, Validation of a MGM1/OPA1 chimeric gene for functional analysis in yeast of mutations associated with dominant optic atrophy, *Mitochondrion.* 25 (2015) 38–48. doi:10.1016/j.mito.2015.10.002.

- [33] T. Ban, J.A.W. Heymann, Z. Song, J.E. Hinshaw, D.C. Chan, OPA1 disease alleles causing dominant optic atrophy have defects in cardiolipin-stimulated GTP hydrolysis and membrane tubulation, *Hum. Mol. Genet.* 19 (2010) 2113–2122. doi:10.1093/hmg/ddq088.
- [34] H. Chen, S.A. Detmer, A.J. Ewald, E.E. Griffin, S.E. Fraser, D.C. Chan, Mitofusins Mfn1 and Mfn2 coordinately regulate mitochondrial fusion and are essential for embryonic development, *J. Cell Biol.* 160 (2003) 189–200. doi:10.1083/jcb.200211046.
- [35] C. Zanna, A. Ghelli, A.M. Porcelli, A. Martinuzzi, V. Carelli, M. Rugolo, Caspase-independent death of Leber's hereditary optic neuropathy cybrids is driven by energetic failure and mediated by AIF and Endonuclease G, *Apoptosis Int. J. Program. Cell Death.* 10 (2005) 997–1007. doi:10.1007/s10495-005-0742-5.
- [36] V. Del Dotto, P. Mishra, S. Vidoni, M. Fogazza, A. Maresca, L. Caporali, J.M. McCaffery, M. Cappelletti, E. Baruffini, G. Lenaers, D. Chan, M. Rugolo, V. Carelli, C. Zanna, OPA1 Isoforms in the Hierarchical Organization of Mitochondrial Functions, *Cell Rep.* 19 (2017) 2557–2571. doi:10.1016/j.celrep.2017.05.073.
- [37] C. Giordano, L. Iommarini, L. Giordano, A. Maresca, A. Pisano, M.L. Valentino, L. Caporali, R. Liguori, S. Deceglie, M. Roberti, F. Fanelli, F. Fracasso, F.N. Ross-Cisneros, P. D'Adamo, G. Hudson, A. Pyle, P. Yu-Wai-Man, P.F. Chinnery, M. Zeviani, S.R. Salomao, A. Berezovsky, R. Belfort, D.F. Ventura, M. Moraes, M. Moraes Filho, P. Barboni, F. Sadun, A. De Negri, A.A. Sadun, A. Tancredi, M. Mancini, G. d'Amati, P. Loguercio Polosa, P. Cantatore, V. Carelli, Efficient mitochondrial biogenesis drives incomplete penetrance in Leber's hereditary optic neuropathy, *Brain J. Neurol.* 137 (2014) 335–353. doi:10.1093/brain/awt343.
- [38] U.E. Pesch, B. Leo-Kottler, S. Mayer, B. Jurklies, U. Kellner, E. Apfelstedt-Sylla, E. Zrenner, C. Alexander, B. Wissinger, OPA1 mutations in patients with autosomal dominant optic atrophy and evidence for semi-dominant inheritance, *Hum. Mol. Genet.* 10 (2001) 1359–1368.
- [39] Kaiser C., Michaelis S. and Mitchell A., *Methods in Yeast Genetics: a Laboratory Course Manual.*, (1994).

- [40] S.N. Ho, H.D. Hunt, R.M. Horton, J.K. Pullen, L.R. Pease, Site-directed mutagenesis by overlap extension using the polymerase chain reaction, *Gene*. 77 (1989) 51–59.
- [41] E. Baruffini, F. Serafini, T. Lodi, Construction and characterization of centromeric, episomal and GFP-containing vectors for *Saccharomyces cerevisiae* prototrophic strains, *J. Biotechnol.* 143 (2009) 247–254. doi:10.1016/j.jbiotec.2009.08.007.
- [42] P. Goffrini, T. Ercolino, E. Panizza, V. Giachè, L. Cavone, A. Chiarugi, V. Dima, I. Ferrero, M. Mannelli, Functional study in a yeast model of a novel succinate dehydrogenase subunit B gene germline missense mutation (C191Y) diagnosed in a patient affected by a glomus tumor, *Hum. Mol. Genet.* 18 (2009) 1860–1868. doi:10.1093/hmg/ddp102.
- [43] E. Panizza, T. Ercolino, L. Mori, E. Rapizzi, M. Castellano, G. Opocher, I. Ferrero, H.P.H. Neumann, M. Mannelli, P. Goffrini, Yeast model for evaluating the pathogenic significance of SDHB, SDHC and SDHD mutations in PHEO-PGL syndrome, *Hum. Mol. Genet.* 22 (2013) 804–815. doi:10.1093/hmg/dds487.
- [44] G. Elachouri, S. Vidoni, C. Zanna, A. Pattyn, H. Boukhaddaoui, K. Gaget, P. Yu-Wai-Man, G. Gasparre, E. Sarzi, C. Delettre, A. Olichon, D. Loiseau, P. Reynier, P.F. Chinnery, A. Rotig, V. Carelli, C.P. Hamel, M. Rugolo, G. Lenaers, OPA1 links human mitochondrial genome maintenance to mtDNA replication and distribution, *Genome Res.* 21 (2011) 12–20. doi:10.1101/gr.108696.110.
- [45] M. Nakamura, J. Lin, S. Ueno, R. Asaoka, T. Hirai, Y. Hotta, Y. Miyake, H. Terasaki, Novel mutations in the OPA1 gene and associated clinical features in Japanese patients with optic atrophy, *Ophthalmology*. 113 (2006) 483–488.e1. doi:10.1016/j.ophtha.2005.10.054.
- [46] A. Olichon, G. Elachouri, L. Baricault, C. Delettre, P. Belenguer, G. Lenaers, OPA1 alternate splicing uncouples an evolutionary conserved function in mitochondrial fusion from a vertebrate restricted function in apoptosis, *Cell Death Differ.* 14 (2007) 682–692. doi:10.1038/sj.cdd.4402048.
- [47] M. Ferré, D. Bonneau, D. Milea, A. Chevrollier, C. Verny, H. Dollfus, C. Ayuso, S.

Defoort, C. Vignal, X. Zanlonghi, J.-F. Charlin, J. Kaplan, S. Odent, C.P. Hamel, V. Procaccio, P. Reynier, P. Amati-Bonneau, Molecular screening of 980 cases of suspected hereditary optic neuropathy with a report on 77 novel OPA1 mutations, *Hum. Mutat.* 30 (2009) E692-705.

doi:10.1002/humu.21025.

[48] J.M. Chao de la Barca, D. Prunier-Mirebeau, P. Amati-Bonneau, M. Ferré, E. Sarzi, C. Bris, S. Leruez, A. Chevrollier, V. Desquirit-Dumas, N. Gueguen, C. Verny, C. Hamel, D. Miléa, V. Procaccio, D. Bonneau, G. Lenaers, P. Reynier, OPA1-related disorders: Diversity of clinical expression, modes of inheritance and pathophysiology, *Neurobiol. Dis.* 90 (2016) 20–26.

doi:10.1016/j.nbd.2015.08.015.

[49] M. Zick, S. Duvezin-Caubet, A. Schäfer, F. Vogel, W. Neupert, A.S. Reichert, Distinct roles of the two isoforms of the dynamin-like GTPase Mgm1 in mitochondrial fusion, *FEBS Lett.* 583 (2009) 2237–2243. doi:10.1016/j.febslet.2009.05.053.

[50] M.S. Kane, J. Alban, V. Desquirit-Dumas, N. Gueguen, L. Ishak, M. Ferre, P. Amati-Bonneau, V. Procaccio, D. Bonneau, G. Lenaers, P. Reynier, A. Chevrollier, Autophagy controls the pathogenicity of OPA1 mutations in dominant optic atrophy, *J. Cell. Mol. Med.* (2017).

doi:10.1111/jcmm.13149.

[51] S. Cogliati, C. Frezza, M.E. Soriano, T. Varanita, R. Quintana-Cabrera, M. Corrado, S. Cipolat, V. Costa, A. Casarin, L.C. Gomes, E. Perales-Clemente, L. Salviati, P. Fernandez-Silva, J.A. Enriquez, L. Scorrano, Mitochondrial cristae shape determines respiratory chain supercomplexes assembly and respiratory efficiency, *Cell.* 155 (2013) 160–171.

doi:10.1016/j.cell.2013.08.032.

[52] M. Kircher, D.M. Witten, P. Jain, B.J. O’Roak, G.M. Cooper, J. Shendure, A general framework for estimating the relative pathogenicity of human genetic variants, *Nat. Genet.* 46 (2014) 310–315. doi:10.1038/ng.2892.

LEGENDS TO FIGURES**Figure 1: Fusion-fission proteins in *OPA1* mutated fibroblasts.**

(A) Western blot of OPA1, MFN1, MFN2 and DRP1 expression levels; tubulin was used as a loading control. A representative experiment out of three is shown for MFN1, MFN2 and DRP1. A representative experiment out of six is shown for OPA1. Densitometric analysis of OPA1/tubulin (B) and OPA1 l-/s-forms ratio (C). Data, expressed as % of WT cells ratio, are means \pm SEM (n=6). (B-C) For I382M, R445H and D603H mutations, data are means of two patients with the same mutation. In all panels * and ** denote values significantly different from the WT ($p < 0.05$ and $p < 0.01$, respectively) using Dunnett's multiple comparison test.

Figure 2: Energetic characterization of *OPA1* mutated fibroblasts.

(A) Cellular ATP levels after incubation for 24 and 48h in DMEM-galactose. Data, expressed as % of ATP content at time=0, are means \pm SEM of WT (n=10), mutants (n=6) except for G439V (n=3). (B) OCR of fibroblasts in DMEM-glucose, expressed as pmoles O₂/min normalized for protein content, under basal conditions and after injection of oligomycin (O), carbonyl cyanide 4-(trifluoromethoxy) phenylhydrazone (FCCP; F), rotenone (R) and antimycin A (AA). (C) Basal, ATP-linked, maximal respiration and spare respiratory capacity. (D) Ratio between maximal and ATP-linked respiration. (E) Cell respiratory control ratio (RCR). (B-E) Data are means \pm SEM of WT (n=10), mutants (n=6) except for G439V (n=5). (F) OCR of fibroblasts in DMEM-galactose (24h). The measure was performed in DMEM-galactose medium. (G) Basal, ATP-linked, maximal respiration and spare respiratory capacity. (H) Ratio between maximal and ATP-linked respiration. (F-H) Data are means \pm SD of WT and mutants (n=3). (A-H) For I382M, R445H and D603H mutations, data are means of two patients with the same mutation. (I) CI IGA and western blot analysis of supercomplexes after BN-PAGE of digitonin-solubilized mitochondria. SDHA (CII) was used as a loading control. Supercomplexes composition and single complexes are indicated. SDS-PAGE of SDHA and VDAC used as a loading control. A representative experiment out of

three is shown. Bars indicate that one lane was removed from the blot. (J) Densitometric analysis of CI alone and CI-containing supercomplexes. Data, expressed as % of WT cells ratio, are means \pm SD of three independent experiments.

In all panels * and ** denote values significantly different from the WT ($p < 0.05$ and $p < 0.01$, respectively) using Dunnett's multiple comparison test.

Figure 3: mtDNA content and mitochondrial network morphology of OPA1 mutated fibroblasts.

(A) mtDNA copy number. Data are means \pm SEM of WT ($n=10$), mutants ($n=6$) except for G439V ($n=3$). (B) Representative images captured by fluorescence microscopy of mitochondrial network morphology of fibroblasts labeled with Mitotracker Red. Cells were incubated in DMEM-glucose (C) or for 24h in DMEM-galactose (D); 40 cells for each cell lines in duplicate (2 independent experiments) has been analyzed for controls (5 cell lines, 400 total cells) for each condition; 60 cells for each cell lines in triplicate (2 independent experiments) has been analyzed for mutants (7 cell lines; 180 total cells for the G439V mutation from one patient and 360 total cells for each of the other three mutations from six patients) for each condition. Cells were scored in three categories on the basis of mitochondrial network morphologies: cells with filamentous and interconnected network (filamentous), cells with short filamentous mitochondria (intermediate) and cells with fragmented mitochondria (fragmented). (A, C-D) For I382M, R445H and D603H mutations, data are the means of two patients with the same mutation. Data are means \pm SEM of three independent experiments. In all panels *, ** and *** denote values significantly different from the WT ($p < 0.05$, $p < 0.01$ and $p < 0.001$, respectively) using Dunnett's multiple comparison test.

Figure 4: Biochemical characterization of OPA1 mutated MEFs.

(A) Western blot of OPA1, MFN1, MFN2 and DRP1 expression levels; tubulin was used as a loading control. A representative blot out of three is shown for MFN1, MFN2 and DRP1. A

representative blot out of eight is shown for OPA1. (B) Densitometric analysis of OPA1 l-/s-forms ratio. Data, expressed as % of ISO1 cells ratio, are means \pm SEM (n=8). (C) Cellular ATP levels. Data are means \pm SEM of WT and ISO1 (n=4) and all the other cell lines (n=3). (D) OCR of *OPA1* mutated MEFs, after the injection of oligomycin (O), carbonyl cyanide m-chlorophenyl hydrazone (CCCP; C), rotenone (R) and antimycin A (AA). (E) Basal, ATP-linked, maximal respiration and spare respiratory capacity. (F) Ratio between maximal and ATP-linked respiration. (G) Cell respiratory control ratio (RCR). (H) OCR and extracellular acidification rate (ECAR) ratio. (D-H) Data are means \pm SD of *Opal*^{-/-} (n=2) and all the other cell lines (n=3). * and ** denote values significantly different from the WT (p<0.05 and p<0.01, respectively) using Dunnett's multiple comparison test.

Figure 5: OXPHOS subunits and supercomplexes analysis of OPA1 mutated MEFs.

(A) Western blot of OXPHOS subunits expression levels; actin was used as a loading control. A representative experiment out of five is shown. (B) Densitometric analysis of OXPHOS subunits. Data, expressed as % of ISO1 cells ratio, are means \pm SEM of five independent experiments. (C) CI IGA and Western blot analysis of supercomplexes by BN-PAGE. SDHA (CII) was used as a loading control. Supercomplexes composition and single complexes are indicated. SDS-PAGE of SDHA and VDAC used as a loading control. A representative experiment out of three is shown. Bars indicate that one lane was removed from the blot. (D) Densitometric analysis of CI and CI-containing supercomplexes. Data, expressed as % of ISO1 cells ratio, are means \pm SD of three independent experiments. * and ** denote values significantly different from the WT (p<0.05 and p<0.01, respectively) using Dunnett's multiple comparison test..

Figure 6: mtDNA content and mitochondrial network morphology of OPA1 mutated MEFs.

(A) mtDNA copy number. Data are means \pm SEM of WT n=5, all the other cell lines n=6.

(B) Representative images captured by fluorescence microscopy of mitochondrial network morphology of MEFs incubated in DMEM-glucose, after labeling with Mitotracker Red (C) 60 cells for WT, *Opa1*^{-/-} and ISO1 in duplicate (2 independent experiments) has been analyzed (120 cell for each lines); 40 cells for mutants cell lines in quadruplicate has been analyzed (160 cell for each mutants); cells were scored exactly as described in Fig. 3. Data are means \pm SD. ** and *** denote values significantly different from the WT ($p < 0.01$ and $p < 0.001$, respectively) using Dunnett's multiple comparison test..

Figure 7. Characterization of I382M, G439V, R445H and D603H mutations in yeast

(A) Phenotypic analysis of haploid strains. Serial cell dilutions (5×10^4 , 5×10^3 , 5×10^2 and 5×10^1 cell/spot) of W303-1B Δ *mgm1* strain transformed with *CHIM3* wild type or mutant alleles were spotted on YP medium, supplemented with either 2% glucose and 2% glycerol. Pictures were taken after a 3-days incubation at 28°C. A representative experiment out of three independent clones is shown. (B) Western Blot analysis of OPA1 expression level. VDAC was used as loading control. A representative experiment out of two is shown. Bars indicate that one lane was removed from the blot. (C) Ratio between the l-form and the s-form normalized to the ratio observed in *CHIM3*. Data are means \pm SD. (D) Representative example of the mitochondrial morphotypes in the investigated yeast strains. (E) Mitochondrial morphotypes percentage in haploid strains. 148 to 328 cells for each strain were observed at the microscope as reported in material and methods and classified as filamentous, fragmented or giant relative according to the mitochondrial morphology. ***($p < 0.001$) denotes significance relative to *CHIM3* strain using a 2×2 χ^2 test comparing filamentous vs fragmented+giant mitochondria. (F) Phenotypic analysis of diploid strains. Serial cell dilutions (5×10^4 , 5×10^3 , 5×10^2 and 5×10^1 cell/spot) of DW1.1 strain containing two copies of *CHIM3* wild type (homoallelic diploid), a copy of *CHIM3* wild type plus an empty plasmid (hemiallelic strain) or a *CHIM3* wild type and a mutant *chim3* copy (heteroallelic diploid) were spotted on YP medium,

supplemented with either 2% glucose or 1.5% glycerol-1.5% ethanol. Pictures were taken after a 5-days incubation at 28°C. A representative experiment out of three independent clones is shown. (G) Respiratory activity of homo-, hemi and heteroallelic strains. Values are means \pm SD of three to four independent experiments and have been normalized to the respiratory activity of the homoallelic diploid. *($p < 0.05$) and **($p < 0.01$) using Dunnett's multiple comparison test. (H) Mitochondrial morphotypes percentage in diploid strains. 280 to 551 cells were classified as filamentous, fragmented or giant according to the mitochondrial morphology. ***($p < 0.001$) denotes significance relative to homoallelic strain using a 2×2 χ^2 test comparing filamentous vs fragmented+giant mitochondria.

Figure 8. Characterization of additional OPA1 mutations in yeast

(A) Phenotypic analysis of haploid strains performed as in figure 7A. (B) Western Blot analysis of *CHIM3* expression level as in figure 7B. A representative experiment out of two is shown. (C) Ratio between the l-/s-forms normalized to the ratio observed in *CHIM3*. Data are means \pm SD. (D) Mitochondrial morphotypes percentage in haploid strains measured as in figure 7E, analyzing 143 to 328 cells for each strain (E) Phenotypic analysis of diploid strains carried out as in figure 7F. (F) Respiratory activity of homo-, hemi and heteroallelic strains determined, as in figure 7G, on four to five independent clones. *($p < 0.05$), **($p < 0.01$) and ***($p < 0.001$) using Dunnett's multiple comparison test. (G) Mitochondrial morphotypes percentage in diploid strains as detailed in figure 7H, analyzing 288 to 737 cells for each strain. Measurement for the heteroallelic L593P could not be carried out due to the low growth level of this strain transformed with the mtGFP vector on SC medium.

Figure 9: Modelling of OPA1 mutations.

Ribbon diagram of OPA1 structural model (A) and localization of the mutations here analyzed (B). Left and right panels report OPA1 modelled in the "open" and "close" conformation, respectively.

In A, ribbons are colored from blue in the proximity of the N-terminus to red at the C-terminus, while in panel B the $C\alpha$ of the mutated residues are reported with light blue spheres for the four mutations studied in fibroblasts and MEFs and green spheres for the mutations analyzed also in yeast and MEFs.

Figure 10: Schematic view of the correlation between the amount of mtDNA and the mitochondrial fragmentation with final outcome in the severity of the DOA disease.

In MEFs model, the increase of mitochondrial fragmentation without reduction of mtDNA copy number is associated with mutations causing pure DOA. The complete fragmentation of the mitochondrial network in association with a depletion of mtDNA hallmarks the DOA “plus” phenotype, whereas a severe alteration of network morphology with a mild decrease in mtDNA copy number characterizes mutations causing both pure DOA and DOA “plus”, located in a borderline zone modulated by modifier factors.

Table 1: Summary of *OPA1* mutations with amino acid change, clinical phenotype and pathogenic prediction (CADD phred>20 are considered as pathogenic variants [52]).

DNA MUTATION variant 1	PROTEIN DOMAIN	AMINOACID CHANGE isoform 1	DISEASE	CADD phred
c.869G>A	GTPase	p.R290Q	DOA “plus”	30
c.893G>A	GTPase	p.S298N	DOA “plus”	27.4
c.899G>A	GTPase	p.G300E	DOA	27.7
c.1146A>G	GTPase	p.I382M	DOA	24.4
c.1316G>T	GTPase	p.G439V	DOA “plus”	30
c.1334G>A	GTPase	p.R445H	DOA “plus”	34
c.1345A>C	GTPase	p.T449P	DOA “plus”	28.1
c.1635C>A	Dynamin	p.S545R	DOA	32
c.1778T>C	Dynamin	p.L593P	DOA	29.9
c.1807G>C	Dynamin	p.D603H	DOA	32
c.2354A>G	Dynamin	p.Q785R	DOA	26.9
c.2729T>A	GED	p.V910D	DOA	34

Table 2: Altered readouts of fibroblasts with the indicated *OPA1* mutations

MUTATIONS	mtDNA	ATP ^a	OCR ^b	RCS	NETWORK ^c	ALTERED PHENOTYPES
I382M	No	-60%*	No	No	20%	1
G439V	+50% *	-80%*	No	No	60%	2
R445H	-30% *	-60%*	No	No	50%	3
D603H	No	-100%**	No	No	10%	1

^a Percent increase/decrease after 24h DMEM-galactose vs control fibroblasts

^b OCR in DMEM-glucose

^c Percentage of fibroblasts with fragmented mitochondria in DMEM-galactose

Table 3: Altered readouts of MEFs bearing the indicated *OPA1* mutations

MUTATIONS	mtDNA	ATP ^a	OCR Max/ATPlinked RCR OCR/ECAR	RCS	NETWORK ^b	ALTERED PHENOTYPES
I382M	No	No	No No No	No	No	0
G439V	-50% **	-80%*	-50%** -50%* -60%*	Yes	100%	5
R445H	-50%**	-80%*	-50%** -50%* -60%*	Yes	100%	5
D603H	No	No	No No -40%*	No	60%	2

^a Percent decrease after 16h DMEM-galactose vs wt MEFs

^b Percentage of MEFs with fragmented mitochondria in DMEM-glucose

Table 4: Altered readouts of yeast bearing the indicated *OPA1* mutations compared to haploid strain transformed with *CHIM3* wt or homoallelic *CHIM3* diploid strain

MUTATIONS	Haploid strain					ALTERED PHENOTYPES
	mtDNA ^a	OXIDATIVE GROWTH ^b	RESPIRATORY ACTIVITY ^c	NETWORK ^d	LONG/SHORT ^e	
I382M	-20%	Slightly decreased	-25%	60%	As wt	4 (slightly)
G439V	ND	Absent	NT	0%	4-fold	5
R445H	ND	Absent	NT	0%	2.5-fold	5
D603H	ND	Absent	NT	0%	2.5-fold	5
MUTATIONS	Diploid Strain				ALTERED PHENOTYPES	
	OXIDATIVE GROWTH ^f	RESPIRATORY ACTIVITY	NETWORK ^g	DOMINANT/RECESSIVE ^h		
I382M	As wt	As wt	As wt	Recessive	0	
G439V	Decreased	-36%**	40%	Negative dominant	3	
R445H	Strongly decreased	-40%**	18%	Negative dominant	3	
D603H	Strongly decreased	-44%**	4%	Negative dominant	3	

^a ND: not detectable by qPCR

^b Oxidative growth on YP medium supplemented with 2% glycerol.

^c NT: not tested due to inability to grow on oxidative carbon sources.

^d Percentage of cells with filamentous mitochondria compared to strain with haploid *CHIM3* wt.

^e Fold increase

^f Oxidative growth on SD medium supplemented with ethanol and glycerol

^g Percentage of cells with filamentous mitochondria compared to homoallelic strain.

^h Based on the previous phenotypes on haploid and diploid strains as explained in the text.

Highlights

Fibroblasts, MEFs and yeast define mechanism and pathogenicity of OPA1 mutations
Yeast model provides information on OPA1 mutations dominance/recessivity
MEFs model highlights different degrees of severity associated with OPA1 mutations
MEFs and yeast models operate in parallel to uncover DOA pathophysiology
mtDNA and mitochondrial fragmentation predict the severity of clinical phenotype

ACCEPTED MANUSCRIPT

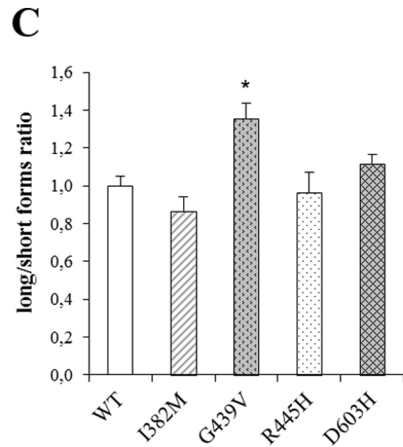
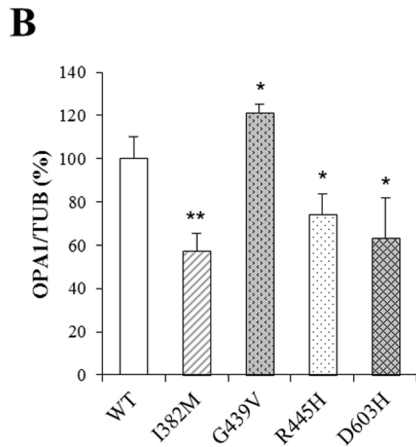
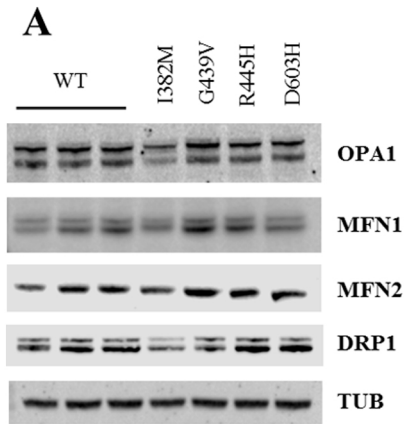


Figure 1

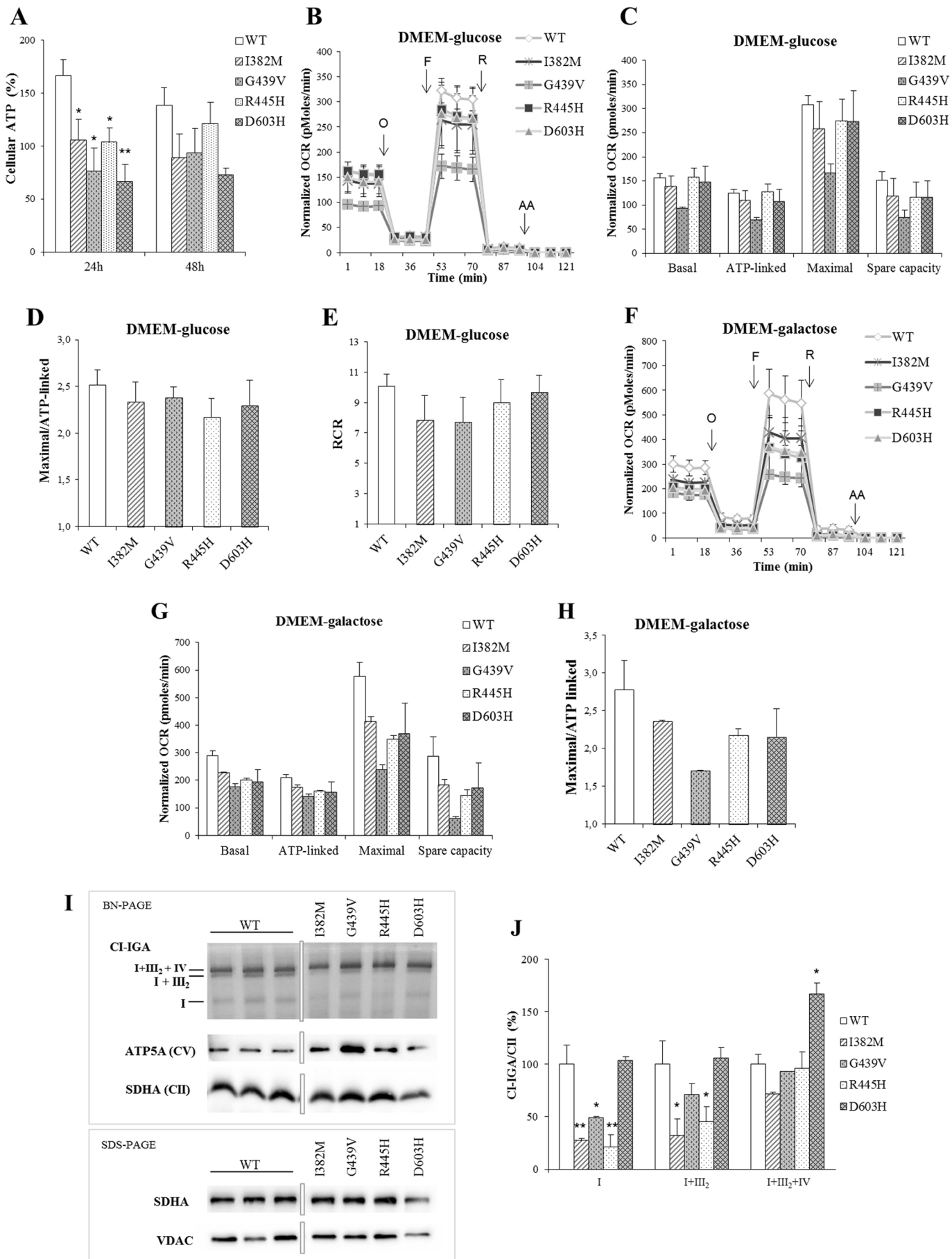


Figure 2

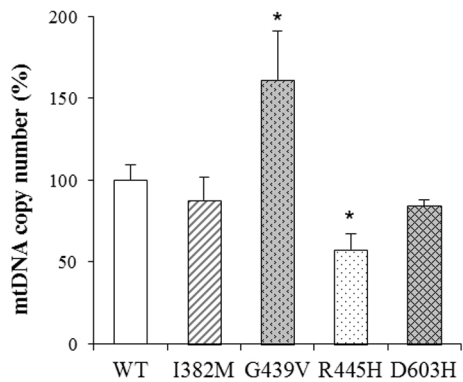
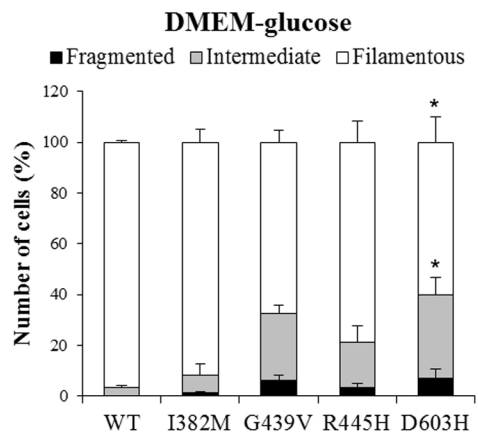
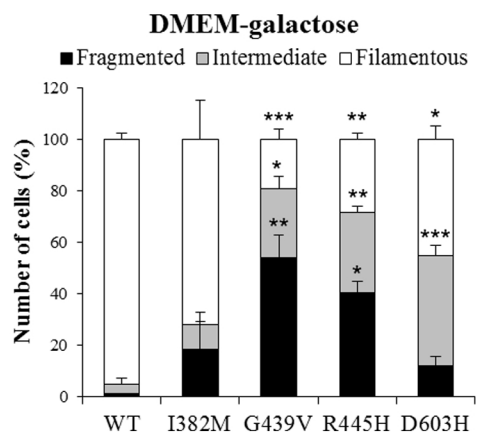
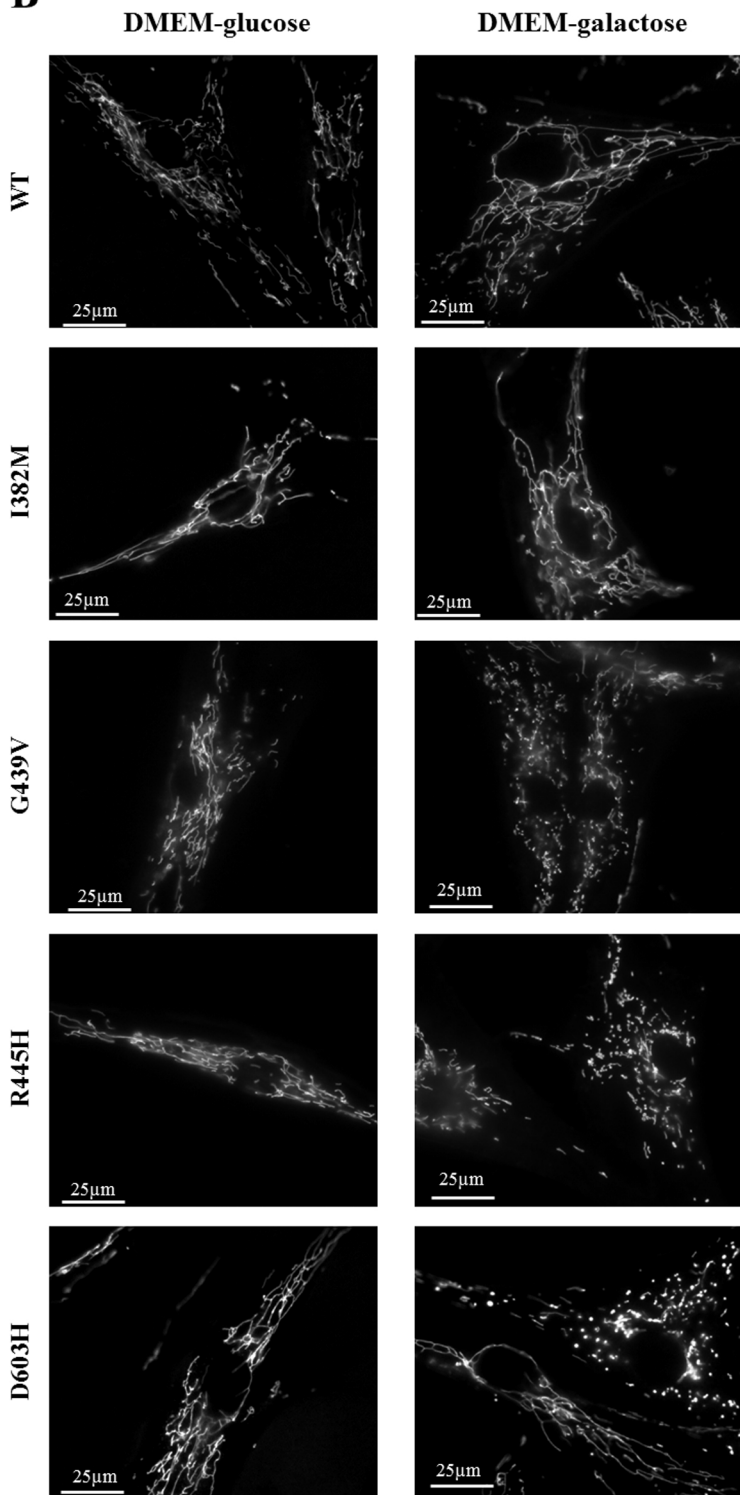
A**C****D****B**

Figure 3

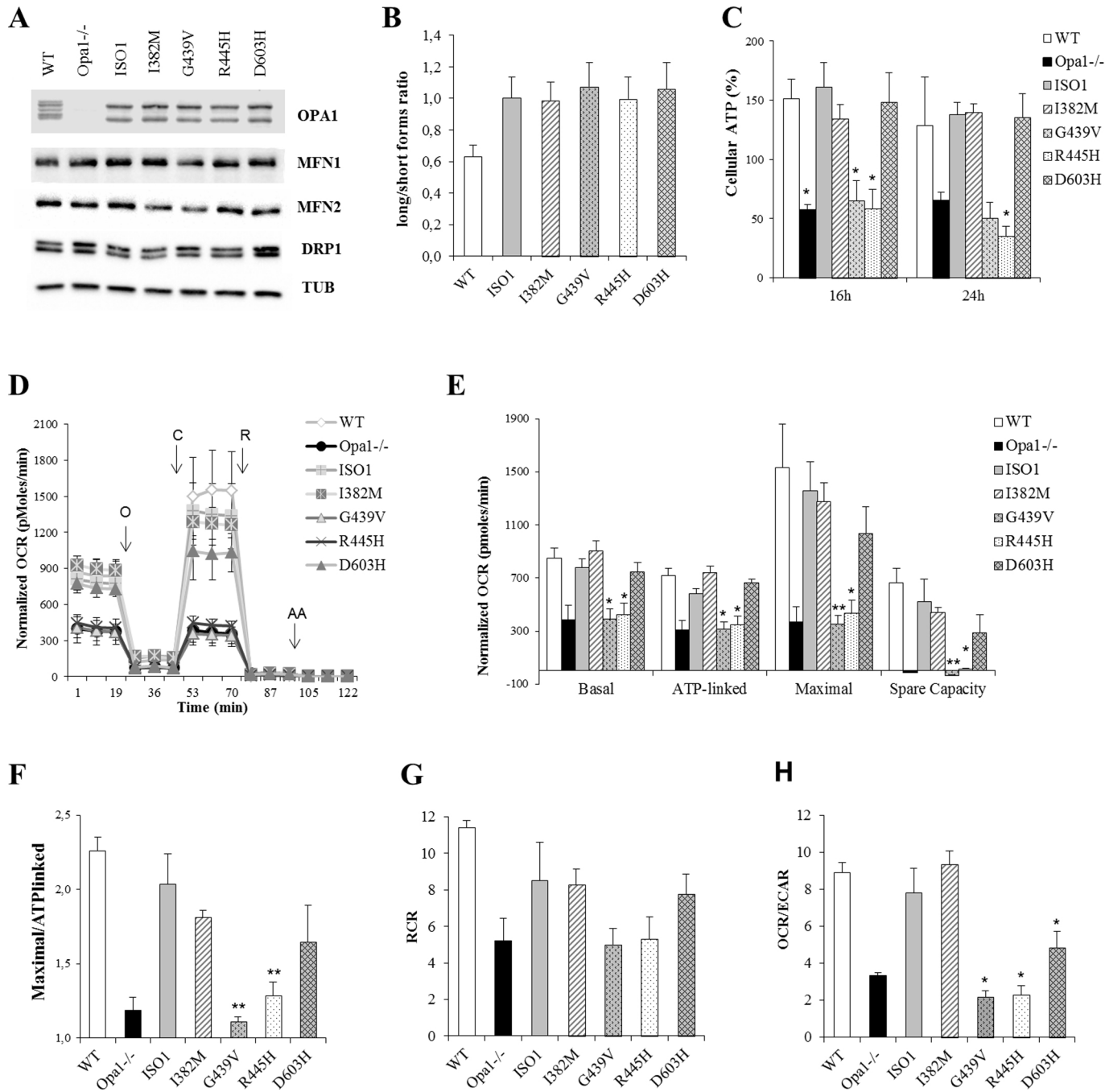


Figure 4

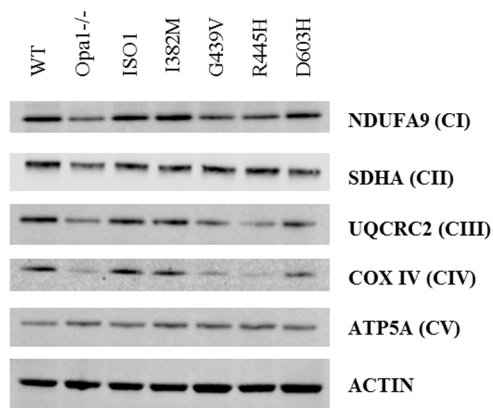
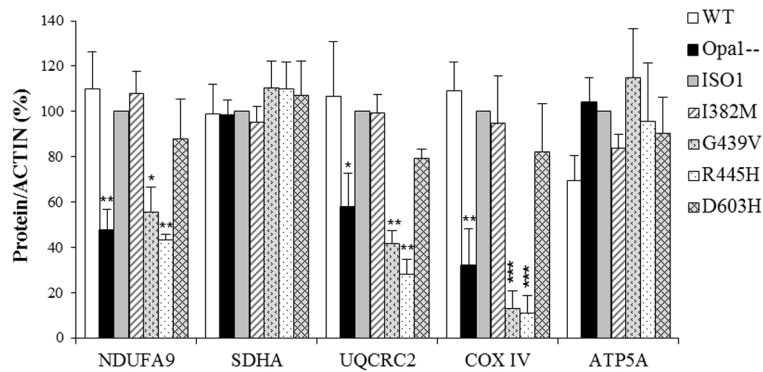
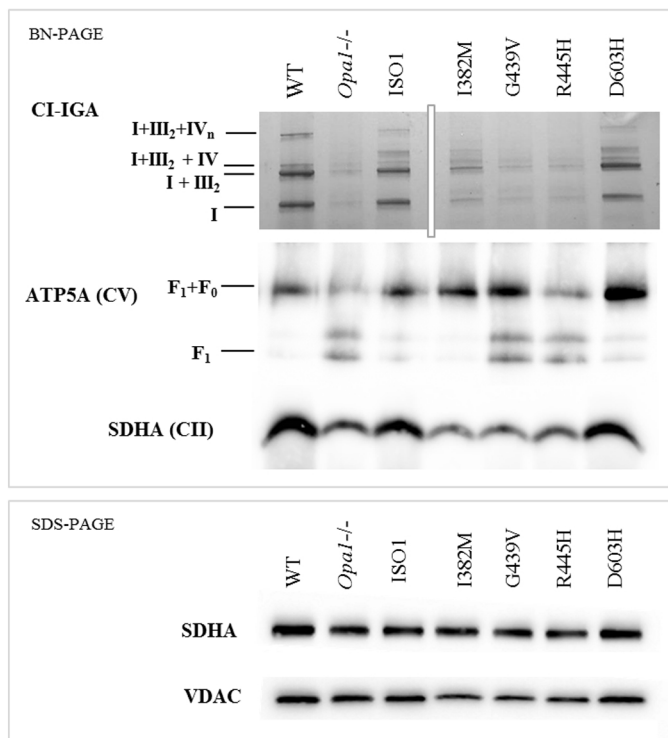
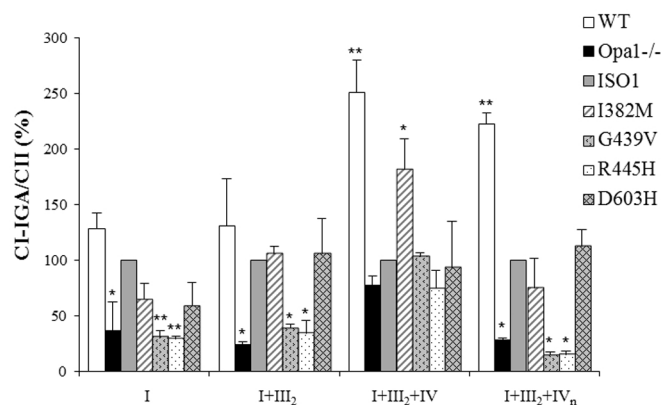
A**B****C****D**

Figure 5

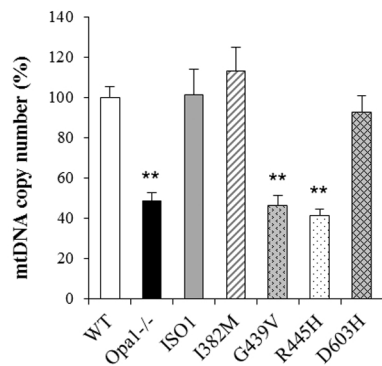
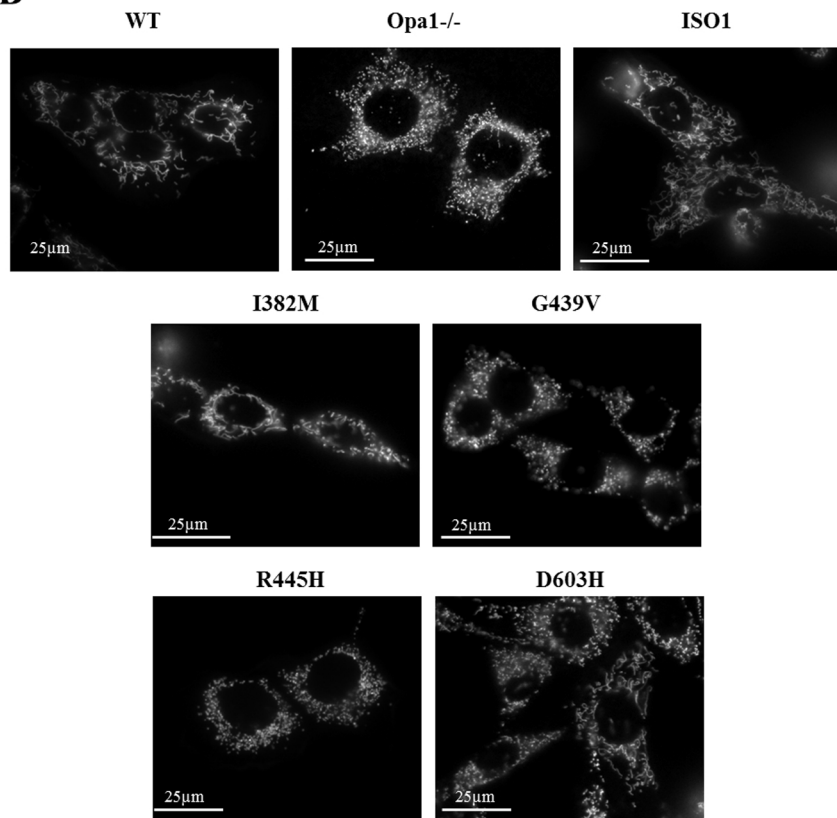
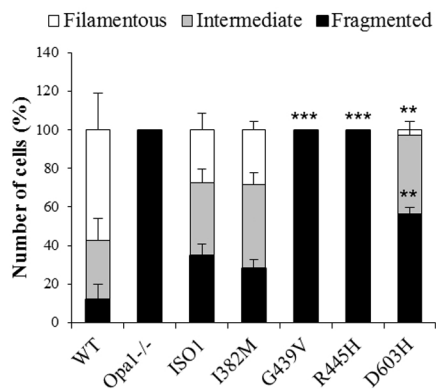
A**B****C**

Figure 6

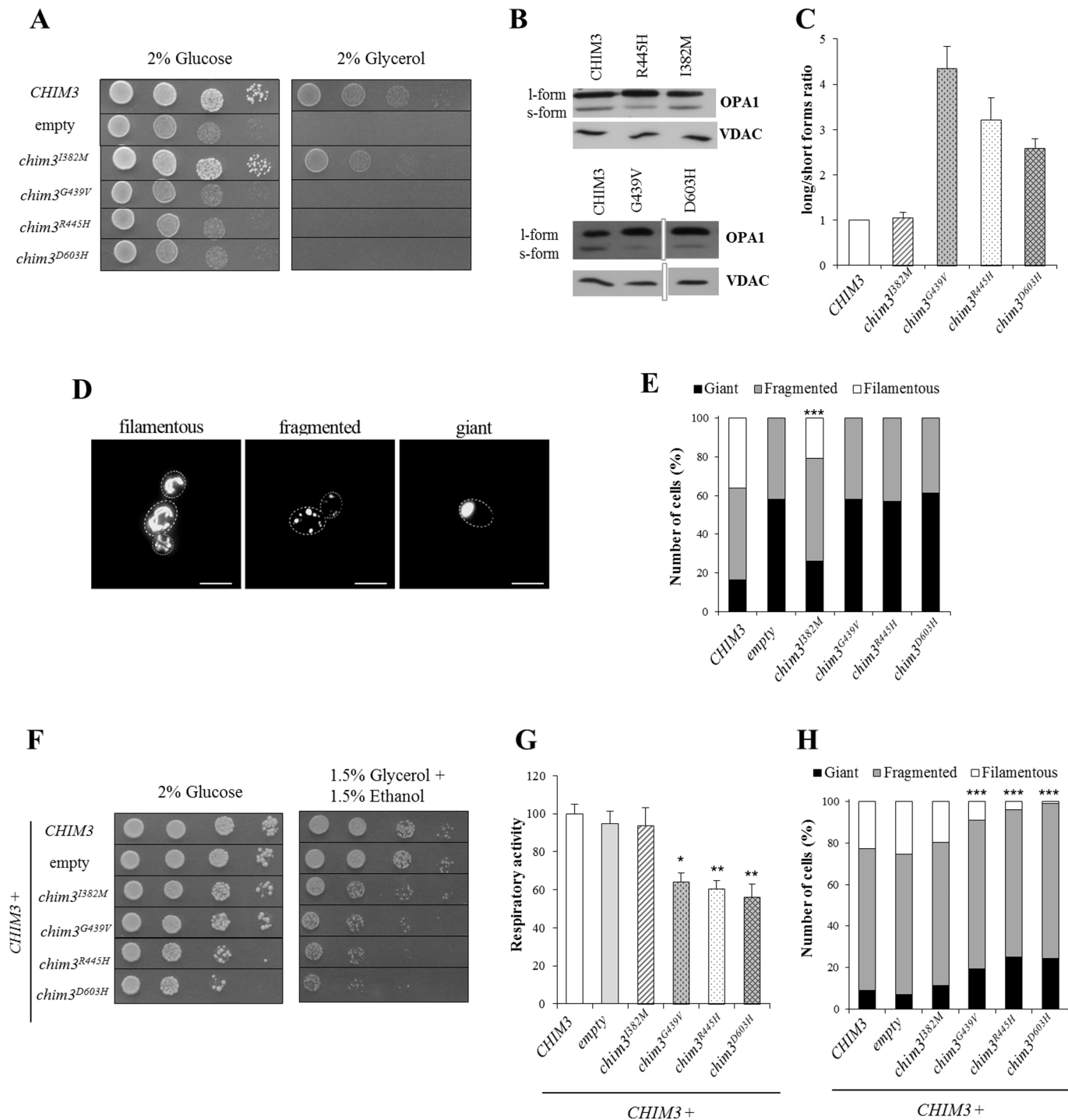


Figure 7

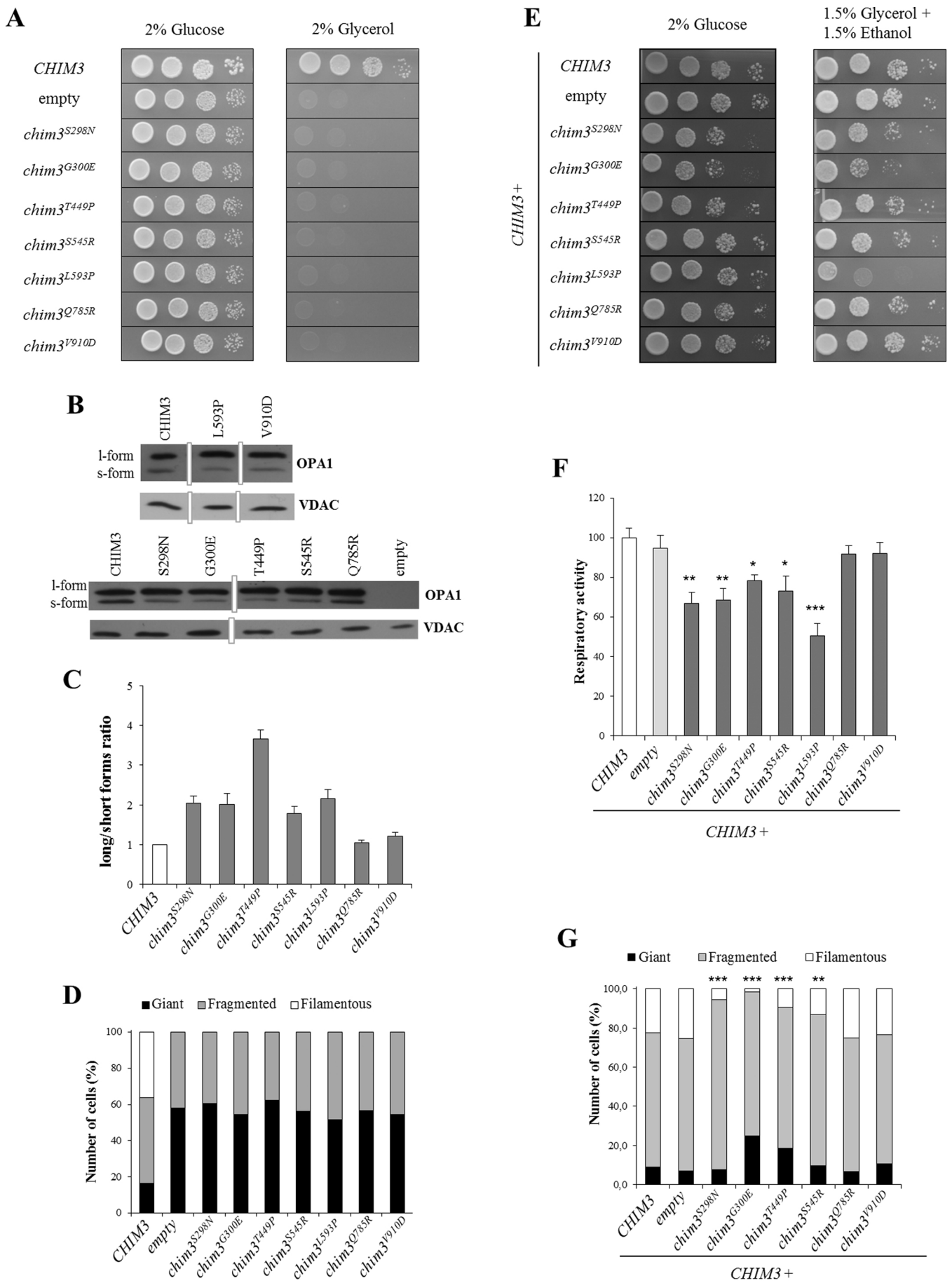


Figure 8

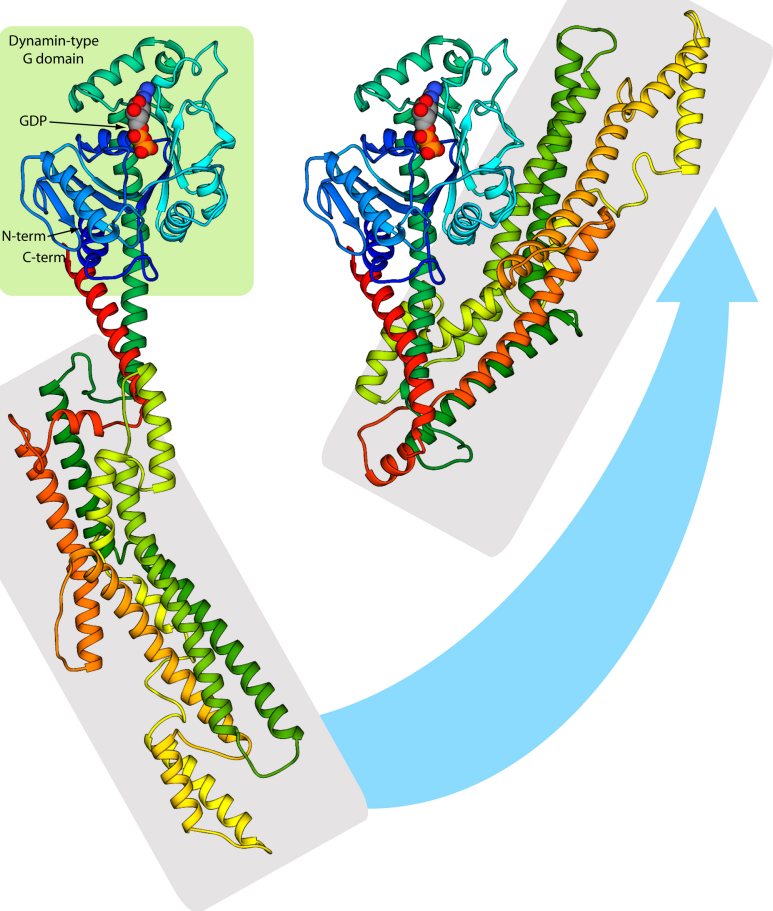
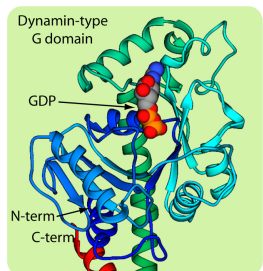
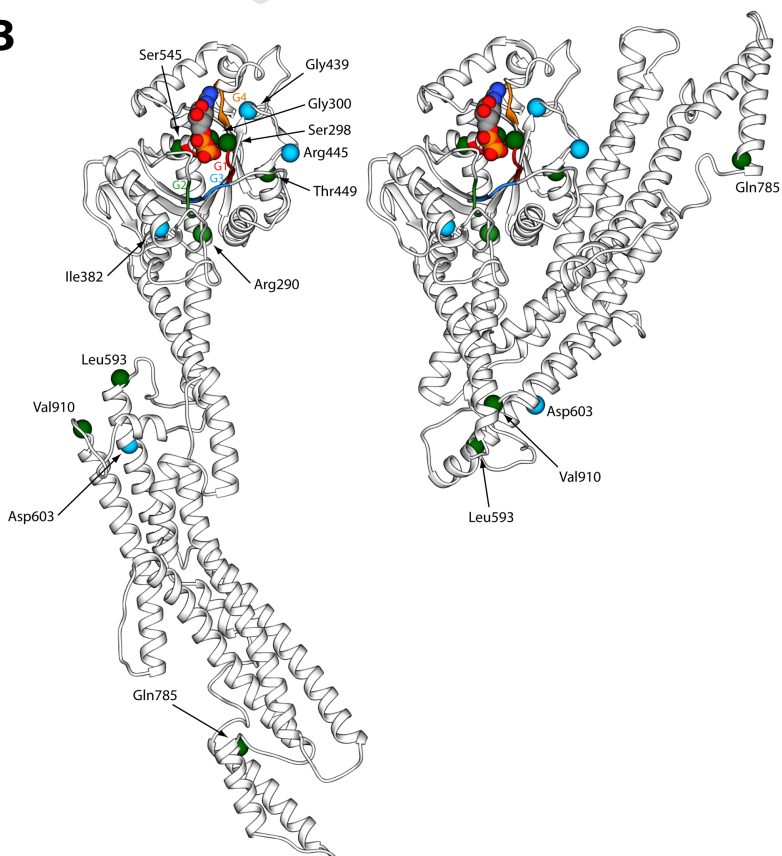
A**B**

Figure 9

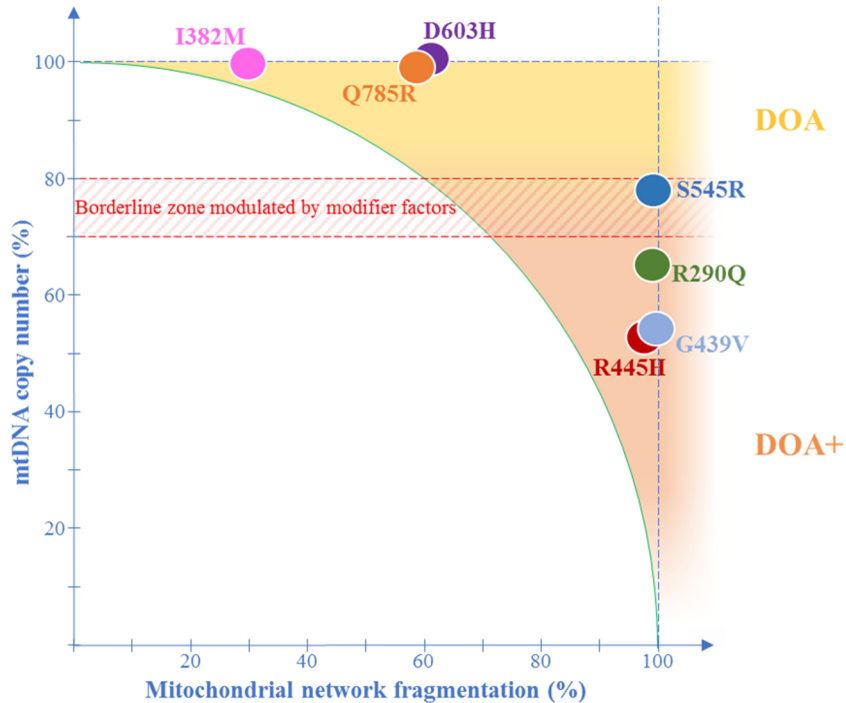


Figure 10